



HAL
open science

In-situ dissolution rates of silicate minerals and associated bacterial communities in the critical zone (Strengbach catchment, France)

Bastien Wild, Damien Daval, Emilie Beaulieu, Marie-Claire Pierret, Daniel Viville, Gwenaël Imfeld

► **To cite this version:**

Bastien Wild, Damien Daval, Emilie Beaulieu, Marie-Claire Pierret, Daniel Viville, et al.. In-situ dissolution rates of silicate minerals and associated bacterial communities in the critical zone (Strengbach catchment, France). *Geochimica et Cosmochimica Acta*, 2019, 249, pp.95-120. 10.1016/j.gca.2019.01.003 . hal-02372322

HAL Id: hal-02372322

<https://hal.science/hal-02372322v1>

Submitted on 20 Nov 2019

HAL is a multi-disciplinary open access archive for the deposit and dissemination of scientific research documents, whether they are published or not. The documents may come from teaching and research institutions in France or abroad, or from public or private research centers.

L'archive ouverte pluridisciplinaire **HAL**, est destinée au dépôt et à la diffusion de documents scientifiques de niveau recherche, publiés ou non, émanant des établissements d'enseignement et de recherche français ou étrangers, des laboratoires publics ou privés.

1 *In-situ* Dissolution Rates of Silicate Minerals and
2 Associated Bacterial Communities in the Critical Zone
3 (Strengbach catchment, France)
4

5 **Bastien Wild^{1,2}, Damien Daval¹, Emilie Beaulieu¹, Marie-Claire Pierret¹, Daniel Viville¹,**
6 **Gwenaël Imfeld¹**

7 *¹Laboratoire d'Hydrologie et de Géochimie de Strasbourg (LHyGeS), Université de*
8 *Strasbourg /EOST-CNRS UMR 7517, 1 Rue Blessig, 67000 Strasbourg, France*

9 *²Andlinger Center for Energy and the Environment, Princeton University, Princeton, NJ*
10 *08544, USA*

11 Corresponding author: bwild@princeton.edu

25 **ABSTRACT**

26 Weathering of silicate minerals in the Critical Zone (CZ) is fundamental for numerous
27 environmental and societal issues. Despite decades of efforts to accurately record
28 biogeochemical variables controlling mineral reactivity in the field and to reproduce them in
29 the laboratory, weathering rates estimates still differ from those observed in natural settings.
30 Here we examine the biogeochemical environment of mineral surfaces exposed to contrasted
31 weathering conditions in various compartments of a temperate CZ (Strengbach observatory,
32 France). A novel approach was developed to probe both *in-situ* mineral dissolution rates and
33 bacterial diversity associated to mineral surfaces. Labradorite and olivine minerals were either
34 buried in the A and C horizons of a soil profile, directly exposed to meteoric fluids or immersed
35 in stream water. Dissolution rates recorded in the soil profile were up to 2 orders of magnitude
36 slower than those predicted using a numerical weathering model. Samples directly exposed to
37 meteoric fluids exhibited contrasted dissolution rates that could not be explained by simple
38 abiotic weathering, while dissolution rates of samples incubated in stream water were
39 particularly low. In soil profiles, the field-laboratory discrepancy by up to 2 orders of magnitude
40 was attributed to heterogeneity of fluid circulation and local variation of reaction conditions.
41 Mineral substrates changed bacterial communities of the mineralosphere after 9 and 20 months
42 of incubation in the CZ. However, we observed that this effect could be delayed or driven by
43 extrinsic factors. Although mineral probes in soil horizons were enriched in bacterial
44 phylotypes potentially involved in mineral weathering (e.g., *Pseudomonas* sp., *Collimonas* sp.,
45 *Burkholderia* sp., *Janthinobacterium* sp., *Leifsonia* sp., and *Arthrobacter* sp.), the relative
46 contribution of biotic weathering could not be quantified *in-situ*. Altogether, the heterogeneity
47 of *in-situ* mineral dissolution rates in key compartments of the CZ reveals the crucial need to
48 improve spatial characterization of hydrogeochemical properties at the soil profile scale, and to
49 evaluate the quantitative role of microbial communities to mineral weathering.

50 1. INTRODUCTION

51 Weathering of primary minerals and associated fluxes involved in elemental cycling in
52 natural settings are relevant for numerous environmental and societal challenges. Important
53 issues include the management of inorganic nutrients stocks in soils with the development of
54 sustainable agricultural and forestry practices (Johnson et al., 2015; Klaminder et al., 2011;
55 Lucas et al., 2011; van der Heijden et al., 2013), the contamination of ecosystems due to mining
56 activities (Yu et al., 2014), or long-term forecast of atmospheric CO₂ concentrations (Beaulieu
57 et al., 2012).

58 Studies on (bio)weathering rates at global (Gaillardet *et al.*, 1999), regional (Gaillardet *et*
59 *al.*, 1995; Negrel *et al.*, 1993), local (Augusto *et al.*, 2000; Feger *et al.*, 1990; Klaminder *et al.*,
60 2011) or micro scales (Bonneville *et al.*, 2016; Fischer *et al.*, 2012; Li *et al.*, 2016) underscore
61 that the knowledge of mineral dissolution rates in the critical zone (CZ) remains incomplete.
62 Field weathering rates are usually determined with indirect methods, such as measurements of
63 U-series nuclides in soils and weathering profiles (Ackerer et al., 2016), the monitoring of
64 changes in solid-state regolith compositions (White et al., 1996) and/or geochemical mass-
65 balances over large space and time scales (Velbel, 1993). These rates are often inconsistent with
66 those measured in the laboratory (White and Brantley, 2003). This “field-lab discrepancy”
67 (Paces, 1983; White and Brantley, 2003; Zhu *et al.*, 2014) has stimulated intensive research to
68 reduce uncertainties on element budgets in natural settings. For instance, several types of
69 indirect field measurement approaches were combined to yield estimates of *in-situ* mineral
70 weathering rates (Ackerer *et al.*, 2016; Ferrier *et al.*, 2010). In parallel, mineral dissolution
71 kinetics were evaluated in the laboratory by monitoring dissolution rates against controlled
72 parameters, such as T, pH or ΔG_r (Carroll and Knauss, 2005; Gruber et al., 2014; Hellmann
73 and Tisserand, 2006). This framework allowed to build up databases of parameters used in
74 semi-empirical mineral weathering rate laws (Palandri and Kharaka, 2004; Rimstidt *et al.*,

75 2012). While this overall strategy has the merit to combine data from independent “top-down”
76 (field measurements) and “bottom-up” (lab experiments) approaches, a consistent theory for
77 mineral weathering in the field is still missing. One possible reason is that “top-down” and
78 “bottom-up” approaches consider different processes, which are recorded on distinct temporal
79 and spatial scales.

80 Most field studies integrate mineral weathering over large space scales, which do not
81 capture the details of the biogeochemical processes at stake. Field studies may thus fail to
82 provide a mechanistic understanding of *in-situ* mineral weathering, although relevant data for
83 past and current weathering in the critical zone have been produced. Estimates of field
84 weathering rates remain, however, several orders of magnitude greater than laboratory
85 estimates that feed common rate laws used in reactive transport models (Maher et al., 2004;
86 White and Brantley, 2003).

87 In addition, inconsistent timescales considered in the laboratory and in the field may result
88 in contrasted mineral dissolution rates due to intrinsic factors, i.e. related to the intrinsic crystal
89 chemistry of the weathered phase, or extrinsic factors, i.e. related to the reacting environment
90 of the crystal (Beig and Luttge, 2006; Gruber et al., 2014; White and Brantley, 2003). Indeed,
91 the physicochemical properties of the fluid/silicate interface may change over time during
92 mineral dissolution, depending on weathering conditions (Daval et al., 2011; Wild et al., 2016).
93 As a result, the dissolution rate of mineral surfaces aged over geologic time scales in the field
94 cannot be directly compared to that of pristine mineral surfaces used in the laboratory, resulting
95 in inconsistent estimates of mineral weathering rates. Moreover, silicate mineral dissolution is
96 too slow under typical field conditions to be measured directly with sufficient accuracy. As a
97 result, most studies on silicate dissolution kinetics have been restricted to the investigation of
98 abiotic, far-from-equilibrium conditions (extreme pH and/or temperature conditions) in

99 laboratory setups. These experimental conditions might change the nature of the elementary
100 processes actually driving mineral dissolution compared to those prevailing in the field.

101 To sum up, (i) mineral dissolution rates measured in the field and in the lab over contrasted
102 time and space scales may not account for the same processes, (ii) local physicochemical
103 environments controlling mineral dissolution rates in the CZ can hardly be probed, and (iii)
104 laboratory conditions, which are generally controlled, homogeneous, constant and abiotic (or
105 which do not involve (multiple) (micro)organisms), might only partly reflect processes ongoing
106 in the field. In that sense, the strict addition of numerous processes observed independently in
107 simple laboratory set-ups (e.g., abiotic, high temperature, short timescales, etc.) may fail to
108 reproduce mineral weathering in natural settings. Nevertheless, parameters derived from
109 laboratory experiments are directly used in reactive transport codes (Gerard *et al.*, 1996; Steefel
110 and Lasaga, 1994; Yeh and Tripathi, 1991) or in chemical weathering models at the catchment
111 scale (Godderis *et al.*, 2006; Sverdrup and Warfvinge, 1995). Current models may thus partly
112 fail to account for extrinsic and intrinsic processes, possibly resulting in a limited agreement
113 between simulation outputs and measurements of field weathering rates.

114 While several models integrate element recycling by vegetation and soil acidity controlled by
115 heterotrophic and autotrophic respiration (Beaulieu *et al.*, 2012; Godderis *et al.*, 2006; Roelandt
116 *et al.*, 2010), the influence of microorganisms on *in-situ* mineral dissolution is currently
117 missing. However, microorganisms have been recognized to interact with mineral substrates
118 (Bennett *et al.*, 1996; Uroz *et al.*, 2009; Uroz *et al.*, 2015), and to impact mineral weathering
119 directly or indirectly. For instance, microorganisms can control locally the thermodynamic
120 activity of species in solution by biofilm production (Barker and Banfield, 1996) or produce
121 organic molecules (either organic acids, ligands or siderophores), which may result in organic-
122 metal chelation (Drever and Stillings, 1997) or ligand-promoted dissolution (Ganor *et al.*, 2009;
123 Welch and Ullman, 1993). Microorganisms can also impact mineral weathering by modifying

124 redox (Lower *et al.*, 2001; Newman and Kolter, 2000; Reguera *et al.*, 2005; Roden *et al.*, 2010)
125 or acid-base conditions (Alisa Mast and Drever, 1987), or even by inducing mechanical stress
126 (Bonneville *et al.*, 2009; Li *et al.*, 2016). The effect of individual microbial strains on mineral
127 weathering has been extensively characterized in controlled systems (Brantley *et al.*, 2001;
128 Kalinowski *et al.*, 2000). However, this approach relies on the selection of culturable strains,
129 which accounts for much less than 1% of the microorganisms occurring in many environments
130 (Solden *et al.*, 2016). Some model microorganisms may thus be selected based on cultivation
131 restrictions (van Scholl *et al.*, 2008) rather than for their actual effect or relevance for mineral
132 weathering. To date, most available bioweathering studies have been considering axenic
133 cultures, with the exception of some recent attempts to use field-relevant microbial
134 communities (Wild *et al.*, 2018). In addition, planktonic cells are generally considered, while
135 biofilms, are often neglected in weathering studies. Altogether, this questions the environmental
136 relevance of experiments conducted with model cultures to infer weathering rates under field
137 conditions. Identifying the weathering potential of microbial communities, as well as their
138 contribution to global weathering fluxes, remains a challenging but fundamental issue that
139 remains largely unexplored.

140 Another important gap between laboratory and field conditions is the consideration of
141 microbial communities in nutrient-poor environments. While microorganisms influence
142 mineral dissolution rates, the mineral substratum may reciprocally influence microbial
143 communities {Bennett, 2001; Certini, 2004; Gleeson, 2005; Gleeson, 2006; Mitchell, 2013;
144 Rogers, 2004; Uroz, 2012; Wild, 2018}. Minerals can thus constitute an ecological niche called
145 the mineralosphere (Uroz *et al.*, 2015). However, factors controlling the interplay between
146 microbial composition and mineral weathering in natural settings remain poorly known.

147 In this context, the purpose of this study was to evaluate *in-situ* mineral dissolution rates in
148 key compartments of the CZ, to assess the physicochemical parameters controlling the

149 dissolution process and to evaluate its impact on bacterial communities. We incubated *in-situ*
150 fresh mineral powders and polished surfaces (i.e., prepared in the laboratory) directly in
151 environmental settings. This approach attempts to bridge field and laboratory measurements by
152 probing *in-situ* (or “on site”) field weathering rates, and by integrating all biotic and abiotic
153 factors contributing to silicate mineral weathering in the field. Mineral dissolution and bacterial
154 communities associated to different types of silicates (see section 2.1) were directly probed in
155 different compartments of the Strengbach Critical Zone Observatory (CZO, Eastern France).
156 Targeted compartments included (i) rocks in open-air weathering conditions (i.e., direct
157 exposure to meteoric fluids), (ii) two contrasted soil compartments (A and C soil horizons), and
158 (iii) the Strengbach stream at the outlet of the watershed. Direct field estimates of mineral
159 weathering rates were compared to rates predicted with the WITCH model (Godderis *et al.*,
160 2006) relying on dissolution rate laws derived from laboratory measurements. This enabled to
161 identify factors contributing to the field-laboratory discrepancy. In parallel, bacterial 16S rRNA
162 gene surveys were conducted using high-throughput sequencing to explore the diversity of
163 microbial communities associated to weathered minerals. Amongst all possible actors for
164 microbial weathering, we focus here on bacteria, whose role in mineral weathering have already
165 been extensively described in literature (see, e.g. Uroz *et al.*, 2015 for a review).

166

167 **2. METHODS**

168 **2.1. Mineral selection**

169 Labradorite, olivine and quartz were selected for this study as model minerals. Labradorite
170 is a tectosilicate belonging to the plagioclase feldspar series, which prevails in the continental
171 crust. Labradorite is a rather reactive feldspar with an approximately halfway composition
172 between albite and anorthite end-members. It contains Na, Ca and some K cations, whose pools
173 may be threatened by some forestry practices in temperate forest ecosystems (Johnson *et al.*,

174 2015; Lucas *et al.*, 2011; van der Heijden *et al.*, 2013). The labradorite used in this study
175 originates from Madagascar and has the following average composition: $\text{Na}_{0.5}\text{Ca}_{0.5}\text{Al}_{1.5}\text{Si}_{2.5}\text{O}_8$
176 (Wild *et al.*, 2016). The olivine used here originates from San Carlos and has a composition
177 close to the pure forsterite pole ($\text{Fo}_{92.0\pm 1.3}$), as determined by inductively coupled plasma atomic
178 emission spectroscopy (ICP-AES) after a standard lithium metaborate fusion. Olivine is a
179 nesosilicate that is characteristic of mafic to ultramafic geological settings. While this mineral
180 is exogenous to the geological context of the study site, it contains Fe and Mg, which are
181 relevant micronutrients in forest ecosystems, and especially for the Strengbach catchment. Fe
182 is a limiting nutrient in most of aerobic natural settings (Johnstone and Nolan, 2015) due to its
183 rapid oxidation kinetics (Davison and Seed, 1983) and its low bioavailability (Saha *et al.*,
184 2013). Deficiency in bioavailable Mg has been reported for the Strengbach CZ (Bonneau *et al.*,
185 1991; Dambrine *et al.*, 1992). Quartz was provided by the Museum of Mineralogy of Strasbourg
186 (France). Quartz is nutrient-free, and it was used in parallel as a non-weatherable reference
187 under the reacting conditions and over the time scales considered (Knauss and Wolery, 1988;
188 Tester *et al.*, 1994).

189

190 **2.2. Study site**

191 Mineral samples were incubated at the Strengbach catchment (Observatoire
192 Hydrog ochimique de l'Environnement, Alsace, France; 48°12'48.33''N; 7°12'2.23''E, 1146
193 m (summit) to 883 m (outlet)), involved French and international critical zone observatories
194 networks (OZCAR, <http://www.ozcar-ri.org/>; RBV,
195 <http://portailrbv.sedoo.fr/?locale=en#CMSConsultPlace:HOME>; CZEN,
196 <http://www.czen.org/content/strengbach-catchment-ohge>). The Strengbach stream drains a
197 surface area of 80 ha (Fig. 1 A). Forested land comprises 80 % of conifers (*Picea abies*), and
198 20% of lobed-leaved trees, dominated by *Fagus sylvatica* spp.

199 The watershed lies on a granitic bedrock, mainly composed of a Hercynian base-poor
200 granite (cordieritic granite) with low Ca and Mg contents, which has been strongly
201 hydrothermally altered on the northern slope and comparatively weakly altered on the southern
202 slope. The top of the northern slope is covered by a 20 to 30 m -thick gneiss layer. Several
203 microgranite intrusions occurred in the southern face (El Gh'Mari, 1995; Pierret *et al.*, 2014).

204 The soils of the watershed range from ochre podzolic soils to brown acidic soils (Lefèvre,
205 1988). Since 1985, the OHGE is fully equipped for continuous monitoring of climatic and
206 hydrogeochemical parameters (Pierret *et al.*, 2014; Viville *et al.*, 2012). Climatic data were
207 obtained from a weather station (Fig. 1 A).

208 The pedological parameters of 10 soil samples collected at the beech plot on 11/18/2013
209 and 12/02/2014 were analyzed at INRA, Arras, France (Tables A.1-A.4; Fig. 1B). About 1 kg
210 of soil samples was collected at several depths along a 120 cm depth soil profile. Water content
211 was estimated by weighing samples before and after drying at 110°C. Soil samples were
212 quartered and sieved (2 mm) as described in previous studies (Duplay *et al.*, 2014; Lucas *et al.*,
213 2011). Granulometry and organic fractions were determined according to SOL-0303 and SOL-
214 0401 standardized procedures, respectively.

215

216 **2.3. Experimental setting**

217 Two sets of mineral probes were incubated simultaneously into four contrasted
218 compartments of the CZ (atmosphere, A and C soil horizons and stream). The mineral probes
219 were collected separately after 9 and 20 months to evaluate temporal changes. Each set of
220 probes consisted of two types of probes: (i) the integrative reactivity probes to estimate *in-situ*
221 dissolution rates of labradorite, olivine and quartz, and (ii) the environmental probes to
222 characterize bacterial communities associated to each mineral.

223

224 2.3.1. *Integrative reactivity probes*

225 The integrative reactivity probes consisted of fresh mineral surfaces of labradorite and
226 olivine prepared by polishing raw materials to eliminate the impact of surface ageing on surface
227 reactivity. A Room Temperature Vulcanizing (RTV) glue mask was deposited on each polished
228 surface to enable direct measurements of the mean mineral weathering rates *in-situ*, integrated
229 over the incubation time, by comparing the topography of the mineral sample before and after
230 incubation (Wild *et al.*, 2016; see also section 2.4). Reactivity of samples is quantified in terms
231 of surface-normalized dissolution rates ($\text{mol.m}^2.\text{s}^{-1}$) throughout this article.

232 Samples were cleaned with ethanol and packed into 100 μm -calibrated mesh nylon cloth
233 (Fisher Scientific, Pittsburgh, PA) to allow circulation of soil fluids and microorganisms. Each
234 nylon bag was individually sealed by sewing with 0.12 mm nylon thread. Bags were sterilized,
235 and DNA was eliminated under UV light and rinsed with 0.2- μm filtrated ethanol. Bags were
236 then dried under laminar flow and kept sterile until incubation at the Strengbach catchment (see
237 Fig. 1-A, and section 2.3.3).

238

239 2.3.2. *Environmental probes*

240 The environmental probes consisted of nylon bags filled up with sterile labradorite, olivine
241 and quartz powders for bacterial colonization. Powder preparation and sterilization was
242 performed as described in Wild *et al.* (2016) and Wild *et al.* (2018). Briefly, olivine, labradorite
243 and quartz crystals were crushed with a hydraulic press, and the powder was dry sieved to
244 recover the 160-315 μm fraction (Fig. A.1). Residual fine particles were removed by successive
245 sonication steps in ethanol, and the removal of particles was assessed by SEM observations.
246 The specific surface area of powders was measured using the Brunauer-Emmet-Teller method
247 (BET, Brunauer *et al.*, 1938). Powders were washed for 10 minutes in sterile vessels with two
248 successive baths of 0.2 μm filtered absolute ethanol, dried for >60 min under sterile laminar

249 flow and exposed to ultraviolet radiation for 20 min. A known amount of powder (2.5-3.5 g)
250 was then sealed in a nylon bag allowing circulation of environmental fluid and microorganisms.
251 Environmental probes were further cleaned and sterilized prior to their incubation at the
252 Strengbach catchment as described previously. Empty control bags were added to each set to
253 evaluate the effect of the nylon bag on bacterial communities.

254

255 *2.3.3. Incubation of the probes in CZ compartments*

256 A first set of probes was fixed to a perforated Polytetrafluoroethylene (PTFE) plate allowing
257 rainfall to flow across the nylon bags (Fig. 1E and 1F). Probes were placed at the weather station
258 (Fig. 1A; 48°13'0.56"N; 7°11'47.82"E). Samples were directly exposed to atmospheric
259 weathering (wind, rainfall and meteoric deposits). This "meteoric" compartment represents the
260 entry point at the atmosphere-soil interface of the CZ, which is not influenced by soil
261 hydrological or pedogenesis processes.

262 Two other sets of probes were incubated into the A-horizon (10-cm depth) and the C-
263 horizon (>60 cm) of the soil profile (Fig. 1B) of the reference beech plot (48°12'41.04"N;
264 7°11'45.66"E). This plot was selected as it combines higher rainfall volumes (northern slope),
265 simple topography (single slope, Fig. 1A) and homogeneous soil and forest covers. Incubation
266 depths corresponded to that of zero-tension lysimetric plates collecting soil solutions since
267 1992. Mean pH of solutions from A-horizon was 4.22 ± 0.17 (1992-2016 period, $n = 178$
268 measurements). In the C horizon, a lower dissolution rate is expected due to higher pH values
269 (mean \pm SD: 4.89 ± 0.28 ; 1992-2016 period, $n = 104$ measurements). Overall, hydrological,
270 geochemical and microbial processes at the A-horizon (topsoil, leaf litter) and the C-horizon
271 (saprolite) are expected to differ.

272 The fourth set was incubated in the Strengbach stream, at the outlet of the watershed
273 (48°13'0.56"N; 7°12'20.95"E), to allow for a permanent fluid-mineral contact. Samples were

274 inserted into PTFE tubes and oriented along stream flow (Fig. 1H and 1I). The average pH of
275 the stream measured at the outlet was 6.46 ± 0.24 for the period of incubation (2014/2015).

276 The sets of probes were collected separately after 9 months (from March 3rd, 2014 to
277 December 2nd, 2014) and 20 months (from March 3rd, 2014 to November 9th, 2015) using sterile
278 forceps. The probes were individually placed into sterile 50 mL Falcon tubes and transported
279 into the laboratory in a sealed cooler and further handled under sterile laminar flow. Probes
280 were collected during the same season (fall) to limit seasonal effects on microbial communities
281 of the mineralosphere (Uroz *et al.*, 2011).

282

283 **2.4. Measurement of mineral weathering rates**

284 Vertical scanning interferometry (VSI, Zygo New View 7300) was used to estimate mineral
285 weathering rates r , based on the global retreat (Δz) of the surface of each integrative reactivity
286 probe after incubation, compared to an unreacted (masked) portion of the same mineral surface,
287 as follows:

$$r = \frac{\Delta z}{\Delta t * V_m} \quad (1)$$

288 where Δt stands for the incubation duration and V_m is the molar volume of the considered
289 mineral. This approach was previously shown to provide dissolution rates consistent with
290 classical powder dissolution experiments (Arvidson *et al.*, 2003; Arvidson and Luttge, 2010;
291 Daval *et al.*, 2013), and has been applied here for the first time in the field.

292

293 **2.5. Predictions of mineral weathering rates**

294 The WITCH model (Godderis *et al.*, 2006) was used to evaluate mineral dissolution rates
295 of samples incubated in soils. The model used physicochemical parameters recorded *in-situ*
296 during mineral incubation. WITCH enabled to reproduce *in-situ* reactivity conditions (e.g.
297 parameters of the reactive fluids including T, pH and more generally, solution composition) at

298 stake during probe incubation using the OHGE database (1987-2016). Modeled mineral
299 dissolution rates relying on kinetic rate laws derived from previous laboratory weathering
300 experiments were compared to *in-situ* measurements based on integrative reactivity probes
301 (field rates). Input parameters of WITCH model such as the solubility products of secondary
302 phases were previously adjusted in a wide variety of contexts (Beaulieu et al., 2012; Beaulieu
303 et al., 2010; Godderis et al.; Violette et al., 2010). Therefore, differences between modeled and
304 observed dissolution rates were interpreted here in terms of field-lab discrepancy.

305 Briefly, the model considered a one-dimensional soil profile discretized into 36
306 homogeneous boxes of 5-cm height overlying a bedrock layer. At each time step, the code
307 solves the following mass-balance equation for each box:

$$\frac{dC}{dt} = F_{up} - F_{down} + F_{weath} - F_{prec} + F_{ex} + F_{veg} \quad (2)$$

308 where C is the concentration of a given dissolved species in the considered box. F_{up} represents
309 the input flux at the top of the considered box through drainage while F_{down} is the output flow
310 through downward drainage. F_{weath} and F_{prec} stand for the release of a given species from
311 primary minerals through weathering processes or for its consumption by the precipitation of
312 secondary phases, respectively. F_{ex} and F_{veg} stand for the fluxes associated to the exchange of
313 this species with the argilo-humic complex or with the vegetation (either nutrient consumption
314 or organic matter decay), respectively. Input fluxes were estimated by a series of rain gauges
315 and an experimental setup at the beech plot dedicated to throughfall and soil solution collection
316 (Prunier *et al.*, 2015, <http://ohge.unistra.fr/>). Output elemental fluxes from the watershed were
317 quantified by an experimental hutch located at the catchment outlet, where water discharge,
318 solute concentrations, suspended matter and sediments are continuously quantified (Viville *et*
319 *al.*, 2012). Fluxes related to mineral weathering were calculated as follows:

$$F_{weath} = Area_{Min} * \phi_{Min} * SMS * x_{molar} * R_{min} \quad (3)$$

320 where $Area_{Min}$ corresponds to the mineral specific surface area in $m_{mineral}^2 \cdot m_{soil}^{-3}$, ϕ_{Min} stands
 321 for the volumetric proportion of that mineral in the considered soil horizon, x_{molar} is the
 322 stoichiometric coefficient of the element of interest in the considered mineral. SMS refers to
 323 the soil moisture saturation (Sverdrup, 1990; Sverdrup and Warfvinge, 1993; Warfvinge and
 324 Sverdrup, 1992):

$$SMS = \frac{\theta * \rho_{solid}}{\rho_{solid} - \rho_i + \theta * \rho_{water}} \quad (4)$$

325 where ρ_{solid} and ρ_{water} are the density of the soil particles and water respectively ($kg \cdot m^{-3}$), ρ_i
 326 is the bulk density of the soil and θ is the dimensionless soil water content. The water content
 327 of each soil layer and the vertical drainage used by the WITCH model were estimated using the
 328 BILJOU© model (Granier *et al.*, 1999).

329 R_{min} ($mol \cdot m^{-2} \cdot s^{-1}$) is the mineral weathering rate defined as:

$$R_{min} = \left[\sum_i A_{i,min} \cdot \exp\left(\frac{-E_{a,min}^i}{RT}\right) \cdot a_i^{n_{i,min}} \right] (1 - \Omega^S) \quad (5)$$

330 where $A_{i,min}$ ($mol \cdot m^{-2} \cdot s^{-1}$) is the Arrhenius pre-exponential factor, R ($J \cdot mol^{-1} \cdot K^{-1}$) the
 331 gas constant and T (K) the absolute temperature, respectively. $E_{a,min}^i$ ($J \cdot mol^{-1}$) is the activation
 332 energy, a_i the dimensionless ion activity and $n_{i,min}$ the dimensionless reaction order with
 333 respect to the hydrolysis of mineral min by the reactive species i (either H^+ , OH^- , H_2O or an
 334 organic ligand). Ω is the dimensionless mineral saturation index and S is a dimensionless
 335 empirical fitting parameter (Maher *et al.*, 2009) assimilated to a “stoichiometric number”
 336 (Godd ris and Donnadieu, 2009; Godderis *et al.*, 2006) equal to 1 for olivine and to 1/3 for
 337 labradorite according to the WITCH database.

338 The soil mineral specific surface area was estimated from soil texture according to a
 339 parametric law (Sverdrup and Warfvinge, 1995):

$$Area_{Min} = \rho * (8.0 * X_{clay} + 2.2 * X_{silt} + 0.3 * X_{sand}) \quad (6)$$

340 where ρ is the density of the considered soil layer, and X_{clay} , X_{silt} , and X_{sand} correspond to the
341 clay, silt and sand fraction, respectively, with

$$X_{clay} + X_{silt} + X_{sand} = 1 \quad (7)$$

342 Soil texture (different fractions), density and porosity were measured on-site for the superficial
343 and the deep layers (5- and 150 cm-depth respectively). The average composition of top and
344 deep soil layers considered to run simulations were: 15% clay, 19% silt and 66% sand, and 9%
345 clays, 19% silt and 72% sand, respectively (according to Table A.2 and Beaulieu *et al.*, 2016).
346 The mineralogical composition in each box was calculated by linear interpolation of the
347 measured data given above. The relative proportions of olivine and labradorite ($\phi_{olivine}$ and
348 $\phi_{Labradorite}$) were set to 0.001% to make sure that their contribution to the modeled solution
349 composition remains negligible. The flux of exchangeable ions (Ca^{2+} , Mg^{2+} , K^+ , SO_4^{2-} ,
350 HPO_4^{2-} , Al^{3+} et Na^+) was defined following a Fickian diffusion law:

$$\frac{dE_{EC}}{dt} = -k_x(EC_{surf} - EC_{sol}) \quad (8)$$

351 where E_{EC} is the fraction of sites occupied by an exchangeable ion EC , and k_x is a mass transfer
352 coefficient determined according to the literature (Warfvinge and Sverdrup, 1988). EC_{sol} and
353 EC_{surf} are concentrations calculated in the bulk solution and at the surface of the argilo-humic
354 complex, respectively, based on data from the literature (Alveteg, 1998). Element exchanges
355 between vegetation and soil (F_{veg}) were estimated based on carbon net primary production and
356 carbon recycling determined by the Lund-Potsdam-Jena (LPJ) dynamic global vegetation
357 model (Sitch *et al.*, 2003), and from element/carbon ratios established by Redfield (see Drever
358 *et al.*, 1997). Plant nutrient uptake was allowed down to 1.5 m depth (root compartment),
359 whereas elemental release from litter degradation was only allowed in the superficial soil
360 horizon (above 0.5 m depth) (Beaulieu *et al.*, 2012; Beaulieu *et al.*, 2010; Roelandt *et al.*, 2010).
361 Soil acidification from carbon dioxide partial pressure (p_{CO_2}) induced by autotrophic and

362 heterotrophic respiration processes were calculated from climatic data (precipitation,
363 temperature, cloud cover, atmospheric CO_2 concentration) sourced from the OHGE and CRU-
364 TS global databases (Harris *et al.*, 2014). The actual chemical composition of the input solutions
365 (throughfall) as a boundary condition at the top of the soil column at each time step was
366 determined using the dynamic version of the code. The model was calibrated using time series
367 from 1987 to 2015 and comparison of the composition of soil solutions collected from the
368 lysimetric plates with those predicted at the corresponding depth (see Tables A.5 and A.6).
369 Sulfate concentration, which only depends on hydrological parameters due to the absence of
370 weatherable sulfate-bearing phases at the Strengbach watershed, were reproduced for the A-
371 horizon (Table A.5). The temperature profile along the soil column was defined for each box
372 by linear interpolation between surface temperature and temperature at 1.5 m-depth, defined at
373 each time step as the gliding annual mean of surface temperatures.

374 For mineral samples immersed in the Strengbach stream and at the weather station,
375 predicted surface retreats were estimated assuming permanent contact of the mineral with a
376 solution at a pH corresponding to the annual average pH of the stream or of the rainfall,
377 respectively. The solution-mineral interaction was assumed to be constant throughout the
378 incubation period at a temperature corresponding to the annual mean water and air temperature,
379 respectively.

380

381 **2.6. Bacterial community analysis**

382 *2.6.1. DNA extraction*

383 Total DNA was extracted from the soil samples and the stream sediments with a PowerSoil[®]
384 DNA Isolation Kit (MO BIO, Carlsbad, CA, USA) following manufacturer's instructions. DNA
385 extraction were performed on single samples due to limited quantities of incubated powder. The
386 concentrations of DNA were determined using a Qubit[®] Fluorometer and Qubit[®] dsDNA HS

387 Assay Kit (Invitrogen, Carlsbad, CA, USA). A DNA extraction was first carried out from sterile
388 mineral powder before incubation in the CZ compartment. DNA could not be detected in sterile
389 and cleaned samples. Concentrations of DNA extracted from incubated probes ranged from 0.1
390 to 2.1 ng. μL^{-1} for the atmospheric probes, 0.6 to >6 ng. μL^{-1} for the A-horizon probes, 0.1 to >6
391 ng. μL^{-1} for the C-horizon probes, and 3.69 to >6 ng. μL^{-1} for the stream probes.

392

393 *2.6.2. Illumina MiSeq sequencing and data processing*

394 The sequencing procedure has been described previously (Babcsanyi et al., 2017).
395 Sequencing was performed at the Research and Testing Laboratory (Lubbock, TX, USA) using
396 Illumina MiSeq. The 16S rRNA gene spanning hypervariable region V4 was amplified in a
397 two-step process. Forward primer was based on illumina i5 primer (5'-
398 TCGTCGGCAGCGTCAGATGTGTATAAGAGACAG-3') the universal bacterial 515F
399 primer (5'-GTGCCAGCMGCCGCGGTAA-3') (Walters et al., 2011). Corresponding reverse
400 primer was synthesized from illumina i7 primer (5'-
401 GTCTCGTGGGCTCGGAGATGTGTATAAGAGACAG-3') and universal bacterial primer
402 806R (5'-GGACTACHVGGGTWTCTAAT-3'). Sequences were generated by nested
403 polymerase chain reaction (PCR) in 25 μL reactors filled up with 1 μL of 5 μM primer solution
404 and 1 μL of DNA matrix, diluted in a nucleotide-Taq polymerase-MgCl₂ mix. (Qiagen HoStar
405 Taq master mix, Qiagen Inc., Valencia, CA). Reaction was performed in an ABI Veriti
406 incubator (Applied Biosystems, Carlsbad, CA). Reaction products were reamplified by a
407 second PCR step. Primers used in this second step were based on Illumina Nextera sequences:
408 AATGATACGGCGACCACCGAGATCTACAC[i5index]TCGTCGGCAGCGT for the
409 forward and -CAAGCAGAAGACGGCATAACGAGAT[i7index]GTCTCGTGGGCTCGG for
410 the reverse. Generated amplicons were visualized with eGels (Life Technology, Grand Island,
411 NY). Products were divided into several equimolar samples and sorted according to their size

412 by Agencourt AMPure XP (Beckman Coulter, Indianapolis, IN) on a 0.7 ratio basis for each
413 step. DNA concentrations were determined with a Qubit 2.0 spectrofluorometer (Life
414 Technologies, Grand Island, NY) and samples were then loaded in an Illumina MiSeq
415 sequencing device (Illumina Inc., San Diego, CA), equipped with two fluid cells. The data have
416 been deposited with links to BioProject accession number PRJNA492367.

417 Denoising, chimera checking, generation of operational taxonomic units (OTUs) and
418 taxonomic classification were performed using the custom-scripted bioinformatics pipeline of
419 the Research and Testing Laboratory (Lubbock, TX, USA). Based on the sequence identity
420 percentage derived from BLASTn (Altschul et al., 1990), sequences with identity scores to
421 known or well-characterized 16S rRNA gene sequences >97% identity (<3% divergence) were
422 resolved at the species level, >95% to 97% at the genus level, >90% to 95% at the family level,
423 >80% to 90% at the order level, >80 to 85% at the class level and between 77% – 80% at the
424 phylum level. Any match below this identity level was not used in taxonomical analysis.
425 Matrices of taxonomic data were further used to visualize changes in community composition.

426

427 *2.6.3. Bacterial diversity and composition analysis*

428 Principal Coordinate Analyses (PCoA) based on Bray-Curtis dissimilarities (Bray and
429 Curtis, 1957; Odum, 1950) was used to visualize ecological gradients underlying the
430 composition of bacterial communities of the environmental probes. PCoA were performed on
431 R software with the *vegdist* function of the *vegan* package (Okasen *et al.*, 2016). The
432 relationship between community profiles and the proportion of phylotypes in each sample was
433 investigated by *a posteriori* projection of the genera as weighed average of their contribution
434 to the samples onto the PCoA biplot. Discontinuities within the dataset were revealed by
435 applying a Ward hierarchical clustering (Ward, 1963) as an aggregation rule on Bray-Curtis
436 dissimilarities (Bray and Curtis, 1957; Odum, 1950) with the *hclust* function of the *stats*

437 package. Analysis of similarities (ANOSIM) was used to infer statistical differences between
438 bacterial community clusters ($P < 0.01$) whenever possible. Final clusters were selected on the
439 basis of the corresponding average silhouette width. The significance of the axes in each biplot
440 representation was evaluated following Kaiser-Guttman criterion.

441 To calculate the diversity and richness indices, the Illumina MiSeq sequences were re-
442 analyzed using MOTHUR version 1.36.1 (<http://www.mothur.org>) starting from denoised and
443 chimera-checked sequences, aligned, and clustered to define OTUs at 97% sequence identity.
444 Two equivalent datasets were then randomly sub-sampled according to the procedure
445 developed by Schloss *et al* (2009). The resulting datasets were used for rarefaction analysis and
446 to calculate the diversity and richness indices (i.e., Shannon diversity index (H'), inverse
447 Simpson diversity and Chao 1 richness index (S_{chao1}), Babcsanyi *et al.*, 2017).

448

449 **3. RESULTS**

450 **3.1. Soil nutrient pool**

451 Soil physicochemical parameters are provided in Tables A.1-A.4. The profiles of Mg and
452 Ca cationic exchange capacities as a function of depth, which corresponds to inorganic nutrients
453 of interest in the present study, are shown in Fig. 2.

454

455 **3.2. *In-situ* mineral dissolution rates**

456 Topography measurements on crystals incubated at the Strengbach catchment for 9 and 20
457 months enabled to estimate the maximal dissolution rates based on surface retreats or roughness
458 (Tables 1 and 2). The surface retreats for olivine ranged from 1 nm (9.38×10^{-13} mol.m⁻².s⁻¹) to
459 171 nm (7.17×10^{-11} mol.m⁻².s⁻¹), both obtained from the meteoric sets of probes (at the weather
460 station). Overall, upper boundaries of reaction rates for olivine were 3.63×10^{-11} mol.m⁻².s⁻¹

461 (meteoric), $1.20 \times 10^{-11} \text{ mol.m}^{-2}.\text{s}^{-1}$ (soil A horizon), $1.12 \times 10^{-12} \text{ mol.m}^{-2}.\text{s}^{-1}$ (soil C horizon) and
462 $1.70 \times 10^{-12} \text{ mol.m}^{-2}.\text{s}^{-1}$ (stream).

463 For labradorite, surface retreats ranged between 1 nm (stream, C horizon) and 5 nm
464 (stream), corresponding to reaction rates ranging from 1.92×10^{-13} to $2.15 \times 10^{-12} \text{ mol.m}^{-2}.\text{s}^{-1}$. The
465 average upper boundaries of reaction rates for labradorite were $6.21 \times 10^{-13} \text{ mol.m}^{-2}.\text{s}^{-1}$
466 (meteoric), $1.02 \times 10^{-12} \text{ mol.m}^{-2}.\text{s}^{-1}$ (A horizon), $6.20 \times 10^{-13} \text{ mol.m}^{-2}.\text{s}^{-1}$ (C horizon) and 1.37×10^{-12}
467 $\text{mol.m}^{-2}.\text{s}^{-1}$ (stream). Of note, Daval *et al.* (2018) indicated that the measured dissolution rates
468 in the A horizon for labradorite powders incubated for over four years in the same location from
469 2004 to 2008 ($1.9 \times 10^{-12} \text{ mol.m}^{-2}.\text{s}^{-1}$) are similar to those reported above. For some samples, the
470 surface retreat varied significantly along the boundary of the masks (Fig. 3). In such cases,
471 zones with the greatest surface retreats may coincide with zones of preferential fluid circulation,
472 as indicated by material fragments including colluvium or soil sediments (Fig. 3A and 3C
473 (dashed area) and Fig. 4A and 4C (zone 2)). The surface retreats presented in Tables 1 and 2
474 correspond to zones of maximal surface retreat on the crystals where fluid circulation could be
475 evidenced, unless otherwise specified. In addition to global surface retreats (e.g. red arrow, Fig.
476 5C), local dissolution features were detected (e.g. green arrow, Fig. 5C). These non-geometrical
477 “etch pits” were generally randomly aligned and accounted for locally faster dissolution rates
478 (see red color in Fig. 6B, D and E).

479

480 **3.3. Theoretical mineral reactivity**

481 Dissolution rates of olivine and labradorite in the soil profile were primarily controlled by
482 seasonal temperature variations (for both A- and C-horizons, Fig. 7). Simulated pH values of
483 the A horizon (4.3 ± 0.2) was in agreement with observed values (4.37 ± 0.14), whereas
484 simulated values (5.4 ± 0.2) for the C horizon were slightly higher than those observed ($4.83 \pm$
485 0.07). The simulated solution compositions in the A and C horizons corresponded to far-from-

486 equilibrium conditions with respect to both labradorite and olivine (i.e., Ω values close to 0 in
487 equation 5). Based on the transition state theory used in the WITCH model (equation 5), such
488 undersaturation states corresponded to dissolution rates that were virtually not affected by the
489 chemical affinity of the system.

490 For samples from the soil profile, predicted dissolution rates converted into global surface
491 retreats were one to two orders of magnitude greater than rates measured *in-situ* for olivine
492 (Table 2). The laboratory-field discrepancy for dissolution rates in the A horizon varied by a
493 factor of 17 to more than 250 for olivine, and from about 7 to more than 50 for labradorite. In
494 the C horizon, the minimum field-laboratory discrepancy was generally weaker, and ranged
495 from 75 to more than 106 for olivine and from 2 to 7.5 for labradorite.

496 Regarding the set of probes exposed to the atmosphere, the predicted retreat based on the
497 annual average rainfall properties (pH = 5.4; T = 7.1°C) overestimated the maximal measured
498 retreats by a factor of about 2 for labradorite, and up to a factor of 80 for olivine. Of note, a
499 sample of olivine locally exhibited a retreat of 171 nm, which corresponds to a factor of ~ 1 (no
500 laboratory-field discrepancy).

501 For samples incubated in the Strengbach stream, theoretical calculations based on the
502 annual average parameters describing water of the Strengbach stream (pH = 6.5; T = 5.8°C)
503 overestimated the measured values by a factor of 9 to 19 for olivine, and a factor of ≥ 1.8 for
504 labradorite.

505

506 **3.4. Diversification and composition of bacterial communities**

507 *3.4.1. General patterns*

508 An average of 33,719 high-quality sequences (>~250 bp) were obtained for each sample by
509 Illumina MiSeq after analysis with Mothur. The OTUs covered 29 phyla, 322 families and 722
510 genera. Although the sequencing depth (see Fig. A.2 for rarefaction curves) did not

511 systematically allow for a survey of the full extent of bacterial diversity, rarefaction curves of
512 diversity indices reached asymptotes (Fig. A.2). This indicates sufficient sampling depth to
513 capture the diversity of bacterial communities.

514 Bacterial community composition of the soil, the weather station and the stream sets
515 significantly differed ($P < 0.01$), irrespective of the incubation time. Sets incubated at the
516 weather station (Fig. 1G) were the richest in Cyanobacteria (> 18%) and in Bacteroidetes (>
517 22%, Fig. 8), whereas those from the soil (Fig. 1C and D) were enriched in Acidobacteria
518 (>20% horizon 1, > 16%, horizon B). Samples immersed in the stream (Fig. 1J) exhibited a
519 higher mean abundance of Verrucomicrobia.

520 Differences between compartments of the CZ were also observed at the genus level, in
521 particular amongst taxa potentially involved in mineral weathering processes. For instance,
522 highest proportions of OTUs corresponding to *Geobacter* sp., typical from sedimentary
523 environments and involved in Fe(III) reduction through anaerobic respiration (Esther *et al.*,
524 2015), were found in the outlet samples. *Aquabacterium* sp. or *Rhodobacter* sp., which
525 encompass several species known for their iron oxidizing capabilities (Hedrich *et al.*, 2011;
526 Weber *et al.*, 2006), were only found in significant proportions in the stream set of probes.
527 Genera known for their ability to weather iron-bearing silicates through siderophore production
528 such as *Sphingomonas* sp. (Calvaruso *et al.*, 2007; Uroz *et al.*, 2009; Uroz *et al.*, 2007), or
529 identified as dissimilatory iron-reducing bacteria (DIRB), such as *Acidiphilium* sp. (Esther *et*
530 *al.*, 2015) were exclusively found in significant proportions on samples subjected to
531 atmospheric weathering (i.e., at the weather station), especially on olivine samples. Both
532 extracted DNA amounts and diversity indices were larger for the stream sets compared to the
533 soil sets, and generally lower for the sets exposed to the atmosphere (Fig. A.3).

534 3.4.2. A- and C-horizons soil sets

535 Bacterial communities of the A horizon differed significantly from those of the C horizon
536 ($P < 0.01$). Taxa potentially involved in mineral alteration appeared to be unevenly distributed
537 between A and C horizons. For example, phylotype sharing 100% similarity with
538 *Mycobacterium kyorinense* strain KUM 060200 16S ribosomal RNA gene, belonging to the
539 genus *Mycobacterium* associated to biotite alteration within the oak mycorrhizosphere (Uroz *et*
540 *al.*, 2009), was only found in litter samples in relative abundance exceeding 0.1 %.

541 Clustering of samples from both the A and C horizons emphasized distinct communities for
542 mineral probes or environmental matrices (i.e. soil) (Figs. 9 A and 9 C). In the A horizon,
543 bacterial communities from the control empty bags incubated for 9 months, and the quartz
544 samples incubated for 20 months, also differed from the rest of the samples (Fig. 9 D). These
545 samples exhibited lower diversity than other samples from the A horizon, as evidenced by their
546 inverse Simpson (I) and Shannon (H') diversity indices (Fig. A.3 A and B). The richness and
547 bacterial diversity of the olivine sample collected after 20 months of incubation in the A horizon
548 (O20) were higher than for all other samples of the A horizon (Fig. A.3 A and B), and similar
549 to richness and bacterial diversity of corresponding soil sample ($S_{chaol} > 4000$; Fig. A.3 C).

550 Regarding the C-horizon, bacterial communities changed according to both incubation time
551 (9-month samples *versus* 20-month samples, Fig. 9 A) and mineral type (Fig. 9 A). The bacterial
552 diversity indices associated with labradorite and olivine were the highest ($H' > 5$ and $I > 50$)
553 after 20 months of incubation, and close to those of soil samples. Although diversity was on
554 average lower after 9 months, bacterial diversity for labradorite and olivine was systematically
555 larger than that for quartz. The bacterial diversity for labradorite was higher than that of olivine
556 and quartz, although the bacterial richness for labradorite differed from that of other C horizon
557 samples (Fig. A.3 C).

558 *3.4.3 Weather station*

559 Bacterial communities associated with mineral probes exposed to the atmosphere at the
560 weather station were mainly structured according to the mineral type (Fig. 9 A and B). The
561 average bacterial diversity was the lowest among the different sets of this study. The bacterial
562 diversity was the highest for olivine and the lowest for quartz, and significantly increases for
563 olivine between 9 months and 20 months. The olivine sample exhibited the largest specific
564 richness after 20 months of incubation ($S_{chaol} > 2000$, Fig. A.3).

565 3.4.4 Stream sets

566 Bacterial communities from samples immersed in the Strengbach stream differed from
567 those of the related stream sediments (Fig. 9 G). The difference among mineral probes was
568 lower compared to the difference between mineral probes and the stream sediments. Temporal
569 changes in the bacterial communities were observed (Fig. 9 G). The bacterial diversity of
570 environmental probes from the stream was greater than that of probes incubated in other
571 compartments of the CZ ($H' > 6.9$ and $I > 400$, Fig. A.3).

572

573 4. DISCUSSION

574 Dissolution rates of fresh mineral usually retrieved from laboratory experiments generally
575 differ from rates of mineral aged in the field, due to changes in the mineral surface chemistry
576 over geologic time scales. In addition, the biogeochemical weathering environment of minerals
577 in the critical zone is still largely unknown. In this study, we incubated in the field mineral
578 samples comparable to those used in laboratory experiments to identify *in-situ* (i) hotspots of
579 mineral reactivity in the critical zone, (ii) the extent of the field-lab discrepancy, and (iii) main
580 bacterial patterns associated to mineral surfaces. We discuss below the contribution of intrinsic
581 and extrinsic factors to the field-laboratory discrepancy and factors that may be accounted for
582 to limit this discrepancy. Possible effects of bacterial communities on mineral weathering and

583 the effect of extrinsic factors on mineralosphere development in contrasted compartment of the
584 CZ are specifically addressed.

585

586 **4.1. Contribution of intrinsic and extrinsic factors to the field-laboratory** 587 **discrepancy**

588 Field weathering rates of individual minerals are usually determined with indirect methods.
589 In this study, nanoscale topography variations were used to directly probe mineral dissolution
590 rates in the field (Figs. 5,6 and 10). A major finding is that up to two orders of magnitude
591 separate field measurements and laboratory-based predictions (see Tables 1 and 2) from
592 WITCH. Our *in-situ* measurements confirmed lower field weathering rates determined using
593 indirect methods, although fresh surfaces (laboratory-type samples) were used here. The
594 contribution of intrinsic and extrinsic factors to this discrepancy are discussed below.

595 *4.1.1 Contribution of intrinsic surface aging*

596 Surface aging refers to any physicochemical modification of the surface of an altered
597 silicate contributing to the decline of its dissolution rate. Surface aging has long been suggested
598 to be an intrinsic factor that contributes to the field-lab discrepancy (Daval et al., 2017; Daval
599 et al., 2018; Fischer et al., 2012; Gruber et al., 2014; Lüttge et al., 2013; Nugent et al., 1998;
600 White and Brantley, 2003). We designed the present study to ensure that surface aging was
601 unlikely to significantly affect dissolution rates of probed minerals.

602 Indeed, polished mineral surfaces used to probe *in-situ* dissolution rates of fresh silicate
603 surfaces in the field minimized the contribution of intrinsic factors to the field-laboratory
604 discrepancy. Assuming that aging (and the possible formation of passivation layers) requires a
605 minimal portion of mineral surface to be weathered (in agreement with recent studies such as
606 Gin et al. (2015) or Daval et al. (2018)), the reaction progress (ζ) after which it becomes
607 significant (i.e., beyond the uncertainties of the measurement), should be specific to the

608 considered mineral at given conditions. Reaction progress (ξ) quantifies here the extent of the
609 reaction of dissolution (in mol.m⁻²) for either olivine or labradorite. In a recent study, Wild *et*
610 *al.* (2016) reported that the decline of labradorite dissolution rate related to surface ageing was
611 observed for $\xi \geq 2.54 \times 10^{-3}$ mol.m⁻². Regarding olivine, mineral ageing was evidenced in
612 laboratory conditions for $\xi \geq 6.92 \cdot 10^{-2}$ mol.m⁻² (Daval *et al.*, 2011). As reported in Tables 1 and
613 2, the maximum reaction progress expected for labradorite and olivine, calculated as the product
614 of the dissolution rate times the incubation period, reached $\xi = 5.68 \cdot 10^{-4}$ mol.m⁻² (labradorite
615 altered into the A horizon over 20 months) and $\xi = 1.71 \cdot 10^{-2}$ mol.m⁻² (olivine altered into the A
616 horizon over 20 months), respectively, which are below the threshold limit reported above.
617 Hence, any difference between the measured and the modeled reaction rates can be attributed
618 to extrinsic factors. In addition, fresh labradorite powders incubated in the A horizon of the
619 exact same plot for durations exceeding four years were still far from being completely covered
620 with passivating surface layers (Daval *et al.*, 2018), thereby further supporting this assertion.
621 *In-situ* measurements could thus be directly compared with WITCH simulations that rely on
622 kinetic rate laws obtained from laboratory experiments.

623

624 4.1.2 Extrinsic factors in the laboratory-field discrepancy

625 Dissolution rates depend on extrinsic parameters, as emphasized in the simplified version
626 of equation 5, adapted from (Lasaga, 1998):

$$R_{min} = A \cdot \exp\left(\frac{-E_{a,min}^i}{RT}\right) \cdot a_{H^+}^n \cdot f(\Delta G_{r,sil}), \quad (9)$$

627 describing mineral weathering rate R_{min} as a function of temperature T , the Gibbs free energy
628 with respect to silicate (*sil*) dissolution $\Delta G_{r,sil}$, and the pH of the fluid, quantified by the
629 chemical activity of protons ($a_{H^+}^n$). These three parameters are the main extrinsic factors that
630 control the aqueous mineral dissolution rate. Aside from the gas constant R , the other
631 parameters of this equation, such as the Arrhenius pre-exponential factor A , the activation

632 energy $E_{a,min}^i$, and the reaction order n are constants derived from laboratory experiments,
633 which are specific to the considered dissolution reaction.

634 A wide range of values has been reported for each of these three parameters, even for the
635 same mineral (Palandri and Kharaka, 2004). Such disparities in parameter values can lead to
636 significant uncertainties between predicted mineral dissolution rates (Rimstidt *et al.*, 2012).
637 Parameters chosen for the present study were retrieved from Rosso and Rimstidt (2000) data
638 for olivine ($A = 3.467 \text{ mol.m}^{-2}.\text{s}^{-1}$, $E_a = 42.6 \text{ kJ.mol}^{-1}$, and $n = 0.50$) and Palandri and Kharaka
639 (2004) data for labradorite ($A = 0.321 \text{ mol.m}^{-2}.\text{s}^{-1}$, $E_a = 42.1 \text{ kJ.mol}^{-1}$, and $n = 0.63$). These two
640 studies provide a meta-analysis of experimental kinetic data and apply statistical methods to
641 infer the rate parameters reported above. We verified that the corresponding rate laws
642 satisfactorily predict dissolution rates of the labradorite and olivine powders reacted in mixed
643 flow set-ups, using the soil solutions collected from lysimetric plates at the Strengbach
644 catchment (see details in Wild *et al.* (2018)).

645 As temperature is an input parameter of the numerical simulations, it can be ruled out as a
646 factor explaining the field-laboratory discrepancy. Since simulated pH values were either
647 similar to those measured, or slightly higher, the contribution of this parameter to the minimal
648 field-lab discrepancy reported in Tables 1 and 2 is negligible. Hence, the observed field-
649 laboratory discrepancy can be ascribed either to the effect of $\Delta G_{r,sil}$ quantified by the $f(\Delta G_{r,sil})$
650 function, or to the fluid-mineral contact time, which is an implicit condition to equation 9.

651 Surface retreats could only be distinguished in areas where fluid circulation occurred on
652 labradorite and olivine samples (see section 3.2 and Figs. 3 and 4, respectively). This indicates
653 that the temporal and spatial extents of fluid-mineral contact may partly account for the field-
654 laboratory discrepancy. In terms of spatial extent of the fluid-mineral interface, no compact
655 coating of secondary minerals potentially masking significant portion of mineral surface could
656 be observed on mineral surfaces after incubation. This hypothesis was therefore ruled out.

657 The extent of fluid-mineral contact time parameter is, on the other hand, indirectly
658 implemented in WITCH with the soil moisture saturation factor (*SMS*) given in equation 4.
659 *SMS* estimates the proportion of the bulk soil volume saturated with aqueous solution for a
660 given depth, which corresponds to the proportion of minerals that is susceptible to exchange
661 matter with the fluid. However, the *SMS* does not allow to localize fluid circulation zones at
662 the soil profile scale. The discrepancy between the data and the model (Fig. 11) is unlikely to
663 result from the hydrological budget alone since the concentration of conservative tracers, such
664 as sulfate anions, fitted observation for the A-horizon (see section 2.5 and Table A.5). Indeed,
665 surface retreats measured for mineral probes of the stream sets were at best one order of
666 magnitude lower than those estimated with kinetic rate laws derived from laboratory
667 experiments, despite permanent fluid-mineral contact (Tables 1 and 2).

668 Finally, the effect of the Gibbs free energy of reaction on mineral dissolution rate may
669 contribute to explain the field-lab discrepancy. The dependence of mineral dissolution rate on
670 $\Delta G_{r,sil}$ is implemented in WITCH through the $(1 - \Omega)$ term in equation 5, in agreement with
671 the transition state theory (TST), which is equivalent to:

$$f_1(\Delta G_r) = 1 - \left[\exp\left(\frac{\Delta G_r}{RT}\right) \right]^s \quad (10)$$

672 in equation (9). Even though this relation is widely used in reactive transport codes and
673 sometimes successfully applied to reproduce field observations (Godd ris and Donnadi u,
674 2009; Godderis et al., 2006; Violette et al., 2010), it may not be appropriate to describe complex
675 reaction pathways (Gin *et al.*, 2008). For instance, the sum of two parallel reactions, with a
676 transition from far-to-equilibrium to close-to-equilibrium dissolution regime occurring at ΔG_r
677 = -7.5 kcal.mol⁻¹, better described the dissolution kinetics of labradorite (Taylor *et al.*, 2000).
678 To test the effect of the selection of the $f(\Delta G_{r,sil})$ function, the empirical relation of Taylor *et*
679 *al.* (2000) was implemented in WITCH:

$$f_2(\Delta G_r) = \left\{ \begin{array}{l} 0.76 * \left[1 - \exp \left(-1.3 * 10^{-17} * \left(\frac{|\Delta G_r|}{RT} \right)^{14} \right) \right] \\ + 0.24 * \left[1 - \exp \left(-0.35 * \frac{|\Delta G_r|}{RT} \right) \right] \end{array} \right\} \quad (11)$$

680 with the exception of a minor sign correction (the original paper mistakenly indicates -0.24
681 instead of +0.24 for eq. 11). Variations of the f_1 and f_2 functions for the A and C horizons are
682 shown in Fig. 11 A. $\Delta G_{r,sil}$ did not affect labradorite dissolution rate in the soil profile if one
683 considers the f_1 function. In contrast, a significant decrease of the apparent dissolution rate of
684 labradorite in the C horizon occurred using the f_2 function. Regarding the C horizon, changing
685 the $f(\Delta G_{r,sil})$ function for the f_2 function totally resolved the field-laboratory discrepancy for
686 labradorite, as shown by values of $\Delta_{L/F} < 1$ (parenthesis, Table 1) and in agreement with Gruber
687 *et al.*, 2014. For the A-horizon, however, the field-laboratory discrepancy could not be totally
688 explained by the equilibrium term since the discrepancy persisted ($\Delta_{L/F} > 1$). Regarding olivine,
689 in the absence of an alternative function describing the $R_{min} - \Delta G_{r,sil}$ dependence of its
690 dissolution kinetics, the TST-based relation was used by default, although it may not be fully
691 relevant.

692 Overall, this shows that current models may partly fail to capture the effects of both
693 heterogeneity of fluid circulations and local physicochemical conditions on mineral dissolution
694 rates in soils of the CZ. The presence of microorganisms associated to minerals may be one of
695 the factors influencing both fluid circulation and local physicochemical conditions. The
696 relationship between bacterial communities and minerals in various compartments of the CZ is
697 discussed below.

698

699 **4.2. Effect of microorganisms on mineral weathering in the CZ**

700 Amongst other extrinsic parameters, biota has been shown to affect mineral weathering
701 (Ahmed and Holmstrom, 2015; Bonneville *et al.*, 2009; Courty *et al.*, 2010; Li *et al.*, 2016;

702 Uroz *et al.*, 2009). Most strikingly, the weathering rate for the olivine surface incubated for 9
703 months at the weather station were low, corresponding to a retreat < 1 nm (Table 2), whereas
704 the surface incubated for 20 months exhibited an exceptional retreat of up to 172 nm (Fig. 10),
705 corresponding to a field-laboratory discrepancy value of $\Delta_{L/F} = 1$ (no discrepancy, see Table
706 2). Rainwater cannot be considered as the unique weathering agent for olivine because open-
707 air incubation conditions offer rather homogeneous input weathering conditions. Variations of
708 reaction rates are at odds with the exposure of olivine surface to homogeneous reactive fluids
709 at the weather station. In addition, the mineral surface retreat measured after 20 months would
710 virtually corresponds to a permanent interaction of the mineral with a fluid of average
711 composition of the rainwater. This condition is unlikely as the samples incubated at the weather
712 stations were prone to drying-wetting cycles. In addition, permanent fluid interaction is
713 inconsistent with the retreat observed after 9 months of incubation in the same conditions
714 (sample MO9, Table 2). The occurrence of several microorganisms on the meteoric probes
715 supports the hypothesis that organisms contributed to mineral weathering.

716 Microorganisms can also affect locally fluid circulation in soil (Or *et al.*, 2007), which can
717 impact mineral weathering by regulating fluid-mineral contact. More specifically, biofilms can
718 disrupt interactions between mineral surface and bulk fluid and stabilize locally zones of
719 preferential fluid circulation. Here, samples from the A-horizon show that the flow path of the
720 solution can be precisely constrained around the fluid boundary ($\pm 10 \mu\text{m}$, approximate width
721 of the transition zone indicated by dashed lines in Fig. 4G) (Fig. 4D-F). Biofilms may thus
722 subtly control fluid flow and act similarly to the RTV glue used to estimate global surface retreat
723 (dark grey area, Fig. 4C and striped area, Fig. 4D-F and 4H).

724 While biofilm may have increased the dissolution rate of olivine exposed to meteoric fluid
725 or indirectly contributed to the field-lab discrepancy by affecting fluid-mineral contact, direct
726 observation of mineral-microorganism contact is missing to support such hypothesis.

727 Concerning soil compartments, no clear direct evidence of bacterial weathering could be
728 observed despite biological weathering could have been favored by K, Ca and Mg
729 concentrations typical for nutrient-poor pedological systems (van der Heijden *et al.*, 2013). Mg
730 concentrations in the soil profile (Fig. 2) were similar to those observed in a reference forest
731 plot located in the Morvan Mountains (Burgundy, France), which exhibited Mg-deficiency
732 thirty years after clear-cutting native forest (van der Heijden *et al.*, 2013). Moreover, symptoms
733 of forest decline, and Mg and Ca nutritional deficits in trees were already described at the
734 Strengbach catchment (Dambrine *et al.*, 1992). We thus tried to indirectly probe clues possible
735 mineral-bacteria interactions by tracking the development of mineral-specific bacterial
736 communities, and how their composition varied according to the mineral substrates (Jones and
737 Bennett, 2014) or their dissolution rates (Uroz *et al.*, 2012). The influence of minerals on
738 bacterial communities in their direct vicinity and the potential for mineral weathering of
739 bacterial phylotypes found in the environmental probe are discussed below. However, one has
740 to keep in mind that only about 6% of the bacterial phyla are identified by usual taxonomic
741 databases (Solden *et al.*, 2016; Yarza *et al.*, 2014). Therefore, relating weathering fluxes to
742 specific bioweathering bacteria in the field solely based on their phylogenetic affiliation
743 remains an elusive goal. In this exploratory study, the relevance of bacterial diversity as a
744 potential indicator of the mineral-bacteria interactions was evaluated.

745

746 *4.2.1 Establishment of mineral-specific bacterial communities*

747 Our results are consistent with the hypothesis that incubated minerals host specific
748 mineralosphere bacterial communities. Indeed, mineralosphere bacterial communities from the
749 soil profile or the Strengbach stream differed from those of the corresponding bulk soil or
750 stream sediment samples respectively. Similarly, mineral-specific communities from the
751 meteoric sets established according to the mineral type. This is in agreement with previous

752 results obtained with a similar approach using *in-situ* incubation of fresh minerals (Mitchell *et*
753 *al.*, 2013; Uroz *et al.*, 2012), field samples (Gleeson *et al.*, 2006), or microcosms inoculated
754 with microbial consortia from a forest soil (Heckman *et al.*, 2013). This point is highlighted
755 here since the development of mineral-specific bacterial communities may reflect the
756 development of phylotypes adapted to mineral weathering, along with the development of
757 bioweathering processes adapted to the mineral substrate.

758 Interestingly, our results also show that mineralosphere communities changed over time.
759 While previous studies provided “snapshots” of mineralosphere bacterial communities
760 (Mitchell *et al.*, 2013; Uroz *et al.*, 2012), two incubation times were considered in the present
761 approach (9 and 20 months), which constitutes an attempt to address temporal changes of
762 bacterial communities. In the C soil horizon and stream sets of probes, time rather than intrinsic
763 mineral weatherability seemed to constitute a primary factor driving community composition
764 (Fig. 9 E). In probes from the C horizon, bacterial communities associated with olivine and
765 labradorite differed more from those associated with non-reactive samples (quartz) after 20
766 months of incubation than in the initial stages of the mineralosphere formation (i.e., after 9
767 months). This support the idea that the mineralosphere develops according to mineral reactivity
768 under field conditions, even though more probes and replicates in each CZ compartments are
769 necessary to confirm this trend.

770

771 4.2.2. *Influence of extrinsic factors on mineralosphere development*

772 Comparison of environmental probes incubated in the atmospheric, soil and stream
773 compartments of the CZ revealed the effect of extrinsic factors (i.e., not related to the mineral)
774 on mineralosphere bacterial communities. Altogether, the results suggest that the relative
775 contribution of extrinsic *versus* intrinsic factors on the differentiation of bacterial communities

776 increases across CZ compartments, following a meteoric < C-horizon < A-horizon < stream
777 pattern.

778 The meteoric sets of probes were exclusively exposed to atmospheric inputs, which are
779 intermittent and nutrient-poor compared to those recorded in the soil or in the stream. In soils,
780 the hygrometry and cationic inputs may be buffered by secondary mineral phases. By contrast,
781 the composition of the fluid in direct contact with mineral probes in the stream was rapidly
782 controlled by the stream hydrochemistry. In the case of the meteoric sets of probes, the mineral
783 type was expected to largely control the surface environment, and thus the response of bacterial
784 communities. Indeed, the mineral represented the main source of inorganic nutrients and/or
785 toxic elements, such as Al (Jones and Bennett, 2014; Singh et al., 2005). Lower overall bacterial
786 diversity for the meteoric sets of probes compared to other sets, and distinct bacterial
787 communities (Fig. 9 A) and diversity (Fig. A.3) according to the mineral substrate, support this
788 hypothesis. The lower impact of external inputs in the case of meteoric probes may also explain
789 the rapid differentiation of bacterial communities according to the mineral type, regardless of
790 the incubation time.

791 Contrasting with observations from the C horizon and meteoric sets of probes, bacterial
792 communities from the A horizon did not cluster according to mineral type. This may reflect
793 more dynamic conditions in the A horizon with respect to both physicochemical conditions and
794 microbial diversity. This is suggested by heterogeneous flows that were evidenced on the probe
795 surface (Fig. 3 and Fig. 4). In addition, organic matter cycling and bioturbation (Gutiérrez and
796 Jones, 2006) may particularly affect, on the short-term, microorganisms of the A horizon by
797 altering nutrient inputs or physicochemical parameters. This may tremendously confound and
798 delay the response of microbial communities to mineral reactivity.

799 The effect of extrinsic factors was apparently even stronger in the case of the stream probes
800 because fluid circulation directly and continuously impacted the physicochemical

801 characteristics of the incubation environment (T, pH, etc.). This is emphasized by the similar
802 composition of bacterial communities observed amongst samples in the stream set of probes
803 (Fig. 9 H) and the higher bacterial diversity observed on these samples compared to other
804 compartments (Fig. A.3). In this case, continuous inputs of dissolved nutrients and particle-
805 associated biomass (Fig. 1 J) may interfere with the development of the mineralosphere. This
806 may in turn challenge and delay the detection of a mineralosphere effect (i.e., specific bacterial
807 communities associated to specific minerals). Analogous effects were observed in an oceanic
808 context, where minerals incubated close to hydrothermal discharge (providing a continuous
809 input of nutrient from fluids) only served as a solid support on which bacteria could attach,
810 whereas similar minerals located far from these fluids inputs served as Fe source for
811 microorganisms (Henri et al., 2016). As a result, the effect of extrinsic factors on the
812 differentiation of mineralosphere bacterial communities may largely differ among CZ
813 compartments for similar incubation times.

814

815 *4.2.3. Occurrence of potential mineral-weathering bacteria*

816 Potential mineral-weathering bacterial taxa found in the environmental probes included
817 *Pseudomonas* sp., *Collimonas* sp., *Burkholderia* sp., *Janthinobacterium* sp., *Leifsonia* sp., and
818 *Arthrobacter* sp. The occurrence of these taxa underscores the potential for biotic alteration in
819 the mineralospheres of the investigated soils. These taxa were found in higher abundance not
820 only in the sets of probes incubated in the soil profile compared to other compartments (2.1%
821 vs. 0.1% on average, Fig. 12), but also in the mineralosphere compared to the corresponding
822 bulk soil horizons (2.6% vs. 0.2% on average, Fig. 12).

823 *Pseudomonas* sp. dominated the studied mineralospheres, with an average proportion of
824 2.5% for the whole dataset and of 4.5% in the soil samples (< 0.1% for the other compartments
825 of the critical zone). Phylotypes belonging to the *Pseudomonas* genus have been described in

826 the literature for their ability to dissolve biotite (Uroz *et al.*, 2009). For both the A and C
827 horizons of the soil profile, *Pseudomonas* sp. was more abundant on labradorite and olivine
828 samples. The proportion of *Pseudomonas* sp. remained constant over time in samples from the
829 C horizon, whereas it decreased in the A horizon between 9 and 20 months of incubation (Fig.
830 12). This suggests that *Pseudomonas* sp. pioneered the colonization of the mineral probes of
831 the soil sets, and mainly occurred in relation to saprolitic alteration. This may be due to the
832 significance of rock weathering in the C horizon relative to other processes that may affect
833 microbial assemblages in the A horizon (e.g. bioturbation, degradation of organic matter or
834 nutrient cycling).

835 *Collimonas* sp. was also particularly abundant in the soil mineral probes (1.9%) compared
836 to other compartments (< 0.1%). It has long been thought that species belonging to the
837 *Collimonas* genus were bacteria living at the expense of organic exudates produced by fungi of
838 the mycorrhizosphere (de Boer *et al.*, 2004). However, *Collimonas* sp. are also capable of
839 extracting elements, such as iron from biotite (Calvaruso *et al.*, 2007; Uroz *et al.*, 2007), or
840 from granite powders (Lapanje *et al.*, 2012) by the production of siderophores, thus supplying
841 their fungal hosts with inorganic nutrients. In our samples, *Collimonas* sp. was found in a larger
842 proportion in the C horizon (i.e., in contact with the saprolite) than in the organic-rich A
843 horizon.

844 The projection of *Collimonas* sp. found for each of the corresponding PCoA analyses (Fig.
845 9) revealed similar trends for samples from the two soil horizons. *Collimonas* sp. prevailed on
846 quartz and labradorite after 9 months of incubation, whereas it decreases in all samples between
847 9 and 20 months, except for olivine, where it increases over the same period. The decline of
848 *Collimonas* sp. was associated to increasing bacterial diversity in all sets of probes incubated
849 in the soil, except for quartz in the A horizon (Fig. A.3). This suggests that *Collimonas* sp. may

850 first establish at the fungus-rock interface, before specializing in iron extraction through the
851 production of siderophores.

852 In average, *Burkholderia* sp. accounted for 1.0% of the total genera recovered from the
853 probes. *Burkholderia* sp. have been reported to enhance the dissolution of biotite, like some
854 members of the genus *Collimonas* (Calvaruso *et al.*, 2007; Uroz *et al.*, 2007), but also apatite
855 (Lepleux *et al.*, 2012; Mailloux *et al.*, 2009), phosphate minerals (Kim *et al.*, 2005; Vassilev *et*
856 *al.*, 2006), quartz (Ullman *et al.*, 1996), bytownite (Barker *et al.*, 1998; Welch *et al.*, 1999) and
857 other feldspars (Ullman *et al.*, 1996), and more generally granite (Wu *et al.*, 2008) or basalt
858 (Wu *et al.*, 2007). Similarly to *Collimonas* sp., *Burkholderia* sp. was mainly found in soil
859 compartments, especially in the A horizon, in particular associated to the quartz sample
860 incubated for 20 months. The latter sample also exhibits a notably low bacterial diversity ($H' < 5$
861 and $I < 50$, Fig. A.3). *Burkholderia* sp. therefore seems to correspond to "lithophilic" bacteria
862 particularly adapted to the context of the A horizon.

863 *Janthinobacterium* sp., *Leifsonia* sp. and *Arthrobacter* sp., which have been described for
864 their ability to dissolve granite through the production of oxalic acid and hydrogen cyanide
865 (Frey *et al.*, 2010), also belonged to the first decile of most abundant bacterial genera. Biotite
866 dissolution was enhanced by species of the genus *Janthinobacterium* (Uroz *et al.*, 2009).
867 Species belonging to the genus *Arthrobacter* may promote the dissolution of hornblende
868 (Kalinowski *et al.*, 2000), quartz and feldspars (Ullman *et al.*, 1996), including bytownite
869 (Barker *et al.*, 1998; Welch *et al.*, 1999). The proportions of *Leifsonia* sp. and *Arthrobacter* sp.
870 after 9 months was higher in the C horizon compared to the A horizon, whereas the proportions
871 were larger in quartz samples after 20 months in both soil horizons (Fig. 12). *Leifsonia* sp., or
872 *Arthrobacter* sp. may preferentially adapt to environments with a lower influence of extrinsic
873 factors, like in the C horizon compared to the A horizon (see section 4.2.2 and Fig. 12), or to
874 the quartz surface, not releasing any toxic or valuable elements. This results in high apparent

875 proportion for the samples associated to low diversity, such as the quartz samples.
876 *Janthinobacterium* sp. occurred in a larger proportion in probes from the C horizon, in particular
877 on olivine and labradorite probes that bear elements of interest such as Mg, Fe or Ca (Fig. 12).
878 The population decrease between 9 and 20 months of incubation suggests that
879 *Janthinobacterium* sp. may be "lithophilic" and compete with other bacterial processes, as
880 described above.

881 Finally, *Polaromonas* sp., which was previously reported in the context of granite
882 weathering (Frey *et al.*, 2010), was present in high proportions in all sets of probes of the C
883 horizon.

884 Overall, bacterial communities of mineralosphere of the soil profile feature several
885 populations that may be involved in mineral weathering. The distribution of bacterial taxa
886 putatively associated with mineral weathering coincided with the disturbed bacterial pattern of
887 the A horizon. Indeed, extrinsic factors (i.e. factors influencing the bacterial community that
888 are not related to the mineral substrate) may considerably affect the distribution of the taxa
889 potential associated with mineral weathering, such as *Pseudomonas* sp., *Janthinobacterium* sp.,
890 *Leifsonia* sp., or *Arthrobacter* sp. Such disturbances may delay the development of a
891 mineralosphere specific to the mineral type.

892

893 *4.2.4 Do bacteria with weathering ability actively dissolve minerals?*

894 Determining whether microorganisms with known weathering activity and present at the
895 surface of minerals actively contribute to mineral dissolution remains challenging. While to
896 date most of the evidences of bacterial mineral dissolution have been based on microscopic
897 observations (Bennett *et al.*, 2001; Jongmans *et al.*, 1997), this approach is still controversial
898 (Benzerara *et al.*, 2007). Another methodology has been suggested, which considers a linear
899 relationship between *in-situ* weathering rates and bacterial diversity (Uroz *et al.*, 2012). In our

900 case, however, no clear correlation could be established between the extent of mineral
901 weathering and bacterial diversity or enrichment of specific taxa (i.e., *Collimonas* sp.,
902 *Burkholderia* sp., *Pseudomonas* sp., *Janthinobacterium* sp., *Leifsonia* sp., or *Arthrobacter* sp.).
903 However, these specific taxa, which may be functionally related to mineral weathering, do not
904 necessarily express this function, and their occurrence may not necessarily reflect a selective
905 pressure for their bioweathering ability.

906 Nevertheless, regarding samples exposed to open-air weathering at the weather station,
907 bacterial diversity globally increases with increasing mineral weatherability (quartz <
908 labradorite < olivine), irrespective of the mineral incubation time. This supports the clustering
909 of bacterial communities according to the mineral substrate shown in Fig. 9 A. In the A-horizon,
910 the Shannon and inverse Simpson diversity indices are higher for olivine (the most weatherable
911 mineral) incubated 20 months in the A horizon than for all the other mineral samples of this
912 compartment (Fig. A.3). The potential for nutrient mobilization of a given mineral may thus
913 stimulate competition between bioweathering agents and support the development of diverse
914 bacterial communities.

915 Regarding the C horizon, variation in the diversity indices echoes the cluster analysis (Fig.
916 9 E). This stresses the first-order importance of time on the composition of bacterial
917 communities: time prevailed over the type of the mineral in the C horizon. Globally, diversity
918 increased for all three minerals as a function of time. On the other hand, diversity was
919 significantly higher for "reactive" minerals after 20 months of incubation and reached that of
920 the corresponding soil samples (Fig. A.3 A, B). Bacterial richness (Chao 1 index) was only
921 significantly higher for labradorite after 20 months, which reflected the diversification of
922 bacterial communities in the C horizon for minerals. The low differences of bacterial diversity
923 between mineral samples immersed in the Strengbach stream confirms the second-order role
924 played by mineral substrates for this compartment.

925 To conclude, diversity analysis of bacterial communities for samples incubated in the A
926 and C horizons of the soil profile and at the weather station suggests a relationship between
927 microbial community diversity and mineral reactivity. Our results support the hypothesis that
928 mineral substrates, depending on their incubation context, may affect microbial communities
929 in their mineralospheres. Diversity analysis of bacterial communities suggests that potential
930 bioweathering bacteria of the A horizon are preferentially associated to (Mg, Fe)-bearing
931 phases, such as olivine, whereas those of the C horizon are rather associated to feldspars
932 minerals, such as labradorite. However, this study is not fully conclusive as to whether the
933 potential of bacterial weathering is actually expressed. This would require strengthening the
934 statistical significance of the results by increasing the number of probes and replicates on the
935 one hand, and to statistically relate dissolution features to bioweathering processes. To address
936 this issue, future studies may consider imaging spatial distribution of microorganisms on
937 mineral samples, especially by assessing their distance from the surface or from dissolution
938 “hot spots” with confocal laser scanning microscopy. Once microorganisms are located on the
939 mineral surface, possible associated dissolution features of biotic origin may be used to quantify
940 associated “biotic rates” by rate spectra analysis (Fischer et al., 2012), such as that presented
941 on Fig. 6.

942

943 **5. SUMMARY AND CONCLUSIONS**

944 The present study shows that *in-situ* mineral dissolution rates and bioweathering
945 environments of minerals can be directly probed *in-situ* in contrasted compartments of the CZ.
946 This approach is complementary to those already used to estimate mineral weathering rates in
947 the field, as it allows for the estimation of mineral weathering rates over short timescales (from
948 months to years).

949 In spite of the limited number of samples that could be incubated, fundamental parameters
950 to understand mineral dissolution in the CZ were identified. In particular, extrinsic factors may
951 partly explain the gap existing between estimates of silicate dissolution rates obtained in the
952 laboratory and in the field, while potential bioweathering bacteria were found in all CZ
953 compartments. Salient results of the present study can be summarized as follows:

954 1) In A and C soil horizons, simulated dissolution rates converted into global surface
955 retreats were greater by a factor of 1 to 270 for olivine, and of 2 to 54 for labradorite
956 than those measured *in-situ*.

957 2) The heterogeneity of fluid circulation in soil profiles should be accounted for in
958 chemical weathering models as it can significantly affect *in-situ* mineral weathering
959 rates.

960 3) The effect of the Gibbs free energy of reaction on labradorite dissolution rates partly
961 explains the discrepancy between laboratory estimates and field measurements for the
962 A and C soil horizons.

963 4) The nature of the mineral substrate affects bacterial communities of the mineralosphere.
964 This process can however be affected or delayed by extrinsic factors, such as nutrient
965 or biomass inputs mediated by fluid circulation.

966

967 In parallel, our study also raised some issues that need to be explored in the future. Although
968 potential bioweathering bacterial phylotypes were detected on environmental probes incubated
969 in A and C horizons, bioweathering activities could not be proved, and the contribution of
970 bacterial activities to the total weathering flux could not be quantified. The approach proposed
971 in this study may however be generalized to evaluate *in-situ* expression of microbial
972 bioweathering functions (i) to quantify the effect of microbial communities on mineral

973 dissolution rate, and (ii) to gradually include bacteria/mineral interactions in next-generation
974 chemical weathering models.

975 Finally, incubation of a greater number of integrative reactivity probes of various mineral
976 types may help in the future to unravel effective local reaction conditions controlling *in-situ*
977 mineral reactivity in CZ compartments.

978

979 **6. ACKNOWLEDGEMENT**

980 The making of probes and of the experimental setup benefited from the technical support of
981 Lisa Wild and René Wild that are warmly acknowledged. The follow up of the experiment
982 would have not been possible without the help of the OHGE team, and particularly Solenn Cotel
983 and Sylvain Benarioumlil. Authors also wish to thank Michael Heap, Heline Maison and Gilles
984 Morvan for technical assistance and François Guyot for numerous and fruitful discussions that
985 contributed to this manuscript. This work was funded through a grant to Gwenaël Imfeld for
986 the project MicXtreme under the framework of the LabEx G-EAU-THERMIE PROFONDE
987 project ANR-11-LABX-0050, and through a grant to Damien Daval under the framework of
988 the VALVE project (EC2CO-BIOHEFECTION program coordinated by the CNRS–Institut
989 National des Sciences de l’Univers).

990

991

992

993

994

995 **7. REFERENCES CITED**

996

997 Ackerer, J., Chabaux, F., Van der Woerd, J., Viville, D., Pelt, E., Kali, E., Lerouge, C.,
998 Ackerer, P., Roupert, R.D., Negrel, P., 2016. Regolith evolution on the millennial timescale
999 from combined U-Th-Ra isotopes and in situ cosmogenic Be-10 analysis in a weathering profile
1000 (Strengbach catchment, France). *Earth Planet. Sci. Lett.* 453, 33-43.

1001 Ahmed, E., Holmstrom, S.J.M., 2015. Microbe-mineral interactions: The impact of surface
1002 attachment on mineral weathering and element selectivity by microorganisms. *Chem. Geol.*
1003 403, 13-23.

1004 Alisa Mast, M., Drever, J.I., 1987. The effect of oxalate on the dissolution rates of oligoclase
1005 and tremolite. *Geochim. Cosmochim. Acta* 51, 2559-2568.

1006 Altschul, S.F., Gish, W., Miller, W., Myers, E.W., Lipman, D.J., 1990. Basic local
1007 alignment search tool. *J. Mol. Biol.* 215, 403-410.

1008 Alveteg, M., 1998. Dynamics of forest soil chemistry. Ph.D, Lund University.

1009 Arvidson, R.S., Ertan, I.E., Amonette, J.E., Luttge, A., 2003. Variation in calcite dissolution
1010 rates: A fundamental problem? *Geochim. Cosmochim. Acta* 67, 1623-1634.

1011 Arvidson, R.S., Luttge, A., 2010. Mineral dissolution kinetics as a function of distance from
1012 equilibrium - New experimental results. *Chem. Geol.* 269, 79-88.

1013 Augusto, L., Turpault, M.P., Ranger, J., 2000. Impact of forest tree species on feldspar
1014 weathering rates. *Geoderma* 96, 215-237.

1015 Babcsanyi, I., Meite, F., Imfeld, G., 2017. Biogeochemical gradients and microbial
1016 communities in Winogradsky columns established with polluted wetland sediments. *FEMS*
1017 *Microbiol. Ecol.* 93.

1018 Barker, W.W., Banfield, J.F., 1996. Biologically versus inorganically mediated weathering
1019 reactions: Relationships between minerals and extracellular microbial polymers in lithobiotic
1020 communities. *Chem. Geol.* 132, 55-69.

1021 Barker, W.W., Welch, S.A., Chu, S., Banfield, J.F., 1998. Experimental observations of the
1022 effects of bacteria on aluminosilicate weathering. *Am. Miner.* 83, 1551-1563.

1023 Beaulieu, E., Godderis, Y., Donnadieu, Y., Labat, D., Roelandt, C., 2012. High sensitivity
1024 of the continental-weathering carbon dioxide sink to future climate change. *Nat. Clim. Change.*
1025 2, 346-349.

1026 Beaulieu, E., Godderis, Y., Labat, D., Roelandt, C., Oliva, P., Guerrero, B., 2010. Impact
1027 of atmospheric CO₂ levels on continental silicate weathering. *Geochim. Cosmochim. Acta* 74,
1028 A65-A65.

1029 Beig, M.S., Luttge, A., 2006. Albite dissolution kinetics as a function of distance from
1030 equilibrium: Implications for natural feldspar weathering. *Geochim. Cosmochim. Acta* 70,
1031 1402-1420.

1032 Bennett, P.C., Hiebert, F.K., Choi, W.J., 1996. Microbial colonization and weathering of
1033 silicates in a petroleum-contaminated groundwater. *Chem. Geol.* 132, 45-53.

1034 Bennett, P.C., Rogers, J.R., Choi, W.J., 2001. Silicates, silicate weathering, and *Microb.*
1035 *Ecol.* *Geomicrobiol. J.* 18, 3-19.

1036 Benzerara, K., Menguy, N., Banerjee, N.R., Tyliszczak, T., Brown, G.E., Guyot, F., 2007.
1037 Alteration of submarine basaltic glass from the Ontong Java Plateau: A STXM and TEM study.
1038 *Earth Planet. Sci. Lett.* 260, 187-200.

1039 Bonneau, M., Dambrine, E., Nys, C., Range, r.J., 1991. Apports acides et cycles des cations
1040 et de l'azote : quelques reflexions à partir des dispositifs de Monthermé (Ardennes) et d'Aubure
1041 (Vosges). *Sci. du Sol* 29, 125-145.

1042 Bonneville, S., Bray, A.W., Benning, L.G., 2016. Structural Fe(II) oxidation in biotite by
1043 an ectomycorrhizal fungi drives mechanical forcing. *Environ. Sci. Technol.* 50, 5589-5596.

1044 Bonneville, S., Smits, M.M., Brown, A., Harrington, J., Leake, J.R., Brydson, R., Benning,
1045 L.G., 2009. Plant-driven fungal weathering: Early stages of mineral alteration at the nanometer
1046 scale. *Geology* 37, 615-618.

1047 Brantley, S.L., Liermann, L., Bau, M., Wu, S., 2001. Uptake of trace metals and rare
1048 earth elements from hornblende by a soil bacterium. *Geomicrobiol. J.* 18, 37-61.

1049 Bray, R.J., Curtis, J.T., 1957. An ordination of the upland forest communities in
1050 southern Wisconsin. *Ecol. Monogr.* 27, 325-349.

1051 Calvaruso, C., Turpault, M.-P., Leclerc, E., Frey-Klett, P., 2007. Impact of
1052 ectomycorrhizosphere on the functional diversity of soil bacterial and fungal communities from
1053 a forest stand in relation to nutrient mobilization processes. *Microb. Ecol.* 54, 567-577.

1054 Carroll, S.A., Knauss, K.G., 2005. Dependence of labradorite dissolution kinetics on
1055 CO₂(aq), Al(aq), and temperature. *Chem. Geol.* 217, 213-225.

1056 Courty, P.E., Buee, M., Diedhiou, A.G., Frey-Klett, P., Le Tacon, F., Rineau, F.,
1057 Turpault, M.P., Uroz, S., Garbaye, J., 2010. The role of ectomycorrhizal communities in forest
1058 ecosystem processes: New perspectives and emerging concepts. *Soil Biol. Biochem.* 42, 679-
1059 698.

1060 Dambrine, E., Carisey, N., Pollier, B., Granier, A., 1992. Effects of drought on the
1061 yellowing status and the dynamic of mineral elements in the xylem sap of a declining spruce
1062 stand (*Picea abies* Karst.). *Plant Soil* 150, 303-306.

1063 Daval, D., Bernard, S., Rémusat, L., Wild, B., Guyot, F., Micha, J.S., Rieutord, F.,
1064 Magnin, V., Fernandez-Martinez, A., 2017. Dynamics of altered surface layer formation on
1065 dissolving silicates. *Geochim. Cosmochim. Acta* 209, 51-69.

1066 Daval, D., Calvaruso, C., Guyot, F., Turpault, M.-P., 2018. Time-dependent feldspar
1067 dissolution rates resulting from surface passivation: Experimental evidence and geochemical
1068 implications. *Earth Planet. Sci. Lett.* 498, 226-236.

1069 Daval, D., Hellmann, R., Saldi, G.D., Wirth, R., Knauss, K.G., 2013. Linking nm-scale
1070 measurements of the anisotropy of silicate surface reactivity to macroscopic dissolution rate
1071 laws: New insights based on diopside. *Geochim. Cosmochim. Acta* 107, 121-134.

1072 Daval, D., Sissmann, O., Menguy, N., Saldi, G.D., Guyot, F., Martinez, I., Corvisier, J.,
1073 Garcia, B., Machouk, I., Knauss, K.G., Hellmann, R., 2011. Influence of amorphous silica layer
1074 formation on the dissolution rate of olivine at 90°C and elevated pCO₂. *Chem. Geol.* 284,
1075 193-209.

1076 Davison, W., Seed, G., 1983. The kinetics of the oxidation of ferrous iron in synthetic
1077 and natural-waters. *Geochim. Cosmochim. Acta* 47, 67-79.

1078 de Boer, W., Leveau, J.H.J., Kowalchuk, G.A., Gunnewiek, P., Abeln, E.C.A., Figge,
1079 M.J., Sjollem, K., Janse, J.D., van Veen, J.A., 2004. *Collimonas fungivorans* gen. nov., sp
1080 nov., a chitinolytic soil bacterium with the ability to grow on living fungal hyphae. *Int. J. Syst.*
1081 *Evol. Microbiol.* 54, 857-864.

1082 Drever, J.I., Stillings, L.L., 1997. The role of organic acids in mineral weathering.
1083 *Colloids. Surf. A Physicochem. Eng. Asp.* 120, 167-181.

1084 Duplay, J., Semhi, K., Errais, E., Imfeld, G., Babcsanyi, I., Perrone, T., 2014. Copper,
1085 zinc, lead and cadmium bioavailability and retention in vineyard soils (Rouffach, France): The
1086 impact of cultural practices. *Geoderma* 230, 318-328.

1087 El Gh'Mari, A., 1995. Etude minéralogique, pétrophysique et géochimique de la
1088 dynamique d'altération d'un granite soumis au dépôts atmosphériques acides (Bassin Versant
1089 du Strengbach, Vosges, France), PhD. Université Louis Pasteur.

1090 Esther, J., Sukla, L.B., Pradhan, N., Panda, S., 2015. Fe (III) reduction strategies of
1091 dissimilatory iron reducing bacteria. *Korean J. Chem. Eng.* 32, 1-14.

1092 Feger, K.-H., Brahmer, G., Zöttl, H.W., 1990. An integrated watershed/plot-scale study
1093 of element cycling in spruce ecosystems of the black forest. *Water, Air, Soil Pollut.* 54, 545-
1094 560.

1095 Ferrier, K.L., Kirchner, J.W., Riebe, C.S., Finkel, R.C., 2010. Mineral-specific chemical
1096 weathering rates over millennial timescales: Measurements at Rio Icacos, Puerto Rico. *Chem.*
1097 *Geol.* 277, 101-114.

1098 Fischer, C., Arvidson, R.S., Lüttge, A., 2012. How predictable are dissolution rates of
1099 crystalline material? *Geochim. Cosmochim. Acta* 98, 177-185.

1100 Frey, B., Rieder, S.R., Brunner, I., Ploetze, M., Koetzsch, S., Lapanje, A., Brandl, H.,
1101 Furrer, G., 2010. Weathering-associated bacteria from the Damma glacier forefield:
1102 physiological capabilities and impact on granite dissolution. *Appl. Environ. Microbiol.* 76,
1103 4788-4796.

1104 Gaillardet, J., Dupre, B., Allegre, C.J., 1995. A global mass budget applied to the Congo
1105 basin rivers - Erosion rates and continental crust composition. *Geochim. Cosmochim. Acta* 59,
1106 3469-3485.

1107 Gaillardet, J., Dupré, B., Louvat, P., Allègre, C.J., 1999. Global silicate weathering and
1108 CO₂ consumption rates deduced from the chemistry of large rivers. *Chem. Geol.* 159, 3-30.

1109 Ganor, J., Renznik, I.J., Rosenberg, Y.O., 2009. Organics in water-rock interactions,
1110 Thermodynamics and kinetics of water-rock interaction. *Mineralogical Society of America*, pp.
1111 259-369.

1112 Gerard, F., Clement, A., Fritz, B., Crovisier, J.L., 1996. Introduction of transport
1113 phenomena into the thermo-kinetic code KINDIS: The code KIRMAT. *C. R. Acad. Sci., Serie*
1114 *II. Sciences de la Terre et des Planetes* 322, 377-384.

1115 Gin, S., Jegou, C., Frugier, P., Minet, Y., 2008. Theoretical consideration on the
1116 application of the Aagaard-Helgeson rate law to the dissolution of silicate minerals and glasses.
1117 Chem. Geol. 255, 14-24.

1118 Gin, S., Jollivet, P., Fournier, M., Angeli, F., Frugier, P., Charpentier, T., 2015. Origin
1119 and consequences of silicate glass passivation by surface layers. Nat. Commun. 6, 6360.

1120 Gleeson, D.B., Kennedy, N.M., Clipson, N., Melville, K., Gadd, G.M., McDermott,
1121 F.P., 2006. Characterization of bacterial community structure on a weathered pegmatitic
1122 granite. Microb. Ecol. 51, 526-534.

1123 Goddéris, Y., Donnadieu, Y., 2009. Climatic plant power. Nature 460, 40.

1124 Godderis, Y., Francois, L.M., Probst, A., Schott, J., Moncoulon, D., Labat, D., Viville,
1125 D., 2006. Modelling weathering processes at the catchment scale: The WITCH numerical
1126 model. Geochim. Cosmochim. Acta 70, 1128-1147.

1127 Granier, A., Breda, N., Biron, P., Villette, S., 1999. A lumped water balance model to
1128 evaluate duration and intensity of drought constraints in forest stands. Ecol. Model. 116, 269-
1129 283.

1130 Gruber, C., Zhu, C., Georg, R.B., Zakon, Y., Ganor, J., 2014. Resolving the gap between
1131 laboratory and field rates of feldspar weathering. Geochim. Cosmochim. Acta 147, 90-106.

1132 Gutiérrez, J.L., Jones, C.G., 2006. Physical ecosystem engineers as agents of biogeochemical
1133 heterogeneity. BioScience 56, 227-236.

1134 Harris, I., Jones, P.D., Osborn, T.J., Lister, D.H., 2014. Updated high-resolution grids
1135 of monthly climatic observations - the CRU TS3.10 Dataset. Int. J. Climatol. 34, 623-642.

1136 Heckman, K., Welty-Bernard, A., Vazquez-Ortega, A., Schwartz, E., Chorover, J., Rasmussen,
1137 C., 2013. The influence of goethite and gibbsite on soluble nutrient dynamics and microbial
1138 community composition. Biogeochemistry 112, 179-195.

1139 Hedrich, S., Schlomann, M., Johnson, D.B., 2011. The iron-oxidizing proteobacteria.
1140 *Microbiology-Sgm* 157, 1551-1564.

1141 Hellmann, R., Tisserand, D., 2006. Dissolution kinetics as a function of the Gibbs free
1142 energy of reaction: An experimental study based on albite feldspar. *Geochim. Cosmochim. Acta*
1143 70, 364-383.

1144 Henri, P.A., Rommevaux-Jestin, C., Lesongeur, F., Mumford, A., Emerson, D.,
1145 Godfroy, A., Ménez, B., 2016. Structural iron (II) of basaltic glass as an energy source for
1146 zetaproteobacteria in an abyssal plain environment, off the mid Atlantic ridge. *Front. Microbiol.*
1147 6.

1148 Johnson, J., Aherne, J., Cummins, T., 2015. Base cation budgets under residue removal
1149 in temperate maritime plantation forests. *For. Ecol. Manage.* 343, 144-156.

1150 Johnstone, T.C., Nolan, E.M., 2015. Beyond iron: non-classical biological functions of
1151 bacterial siderophores. *Dalton Trans.* 44, 6320-6339.

1152 Jones, A.A., Bennett, P.C., 2014. Mineral microniches control the diversity of
1153 subsurface microbial populations. *Geomicrobiol. J.* 31, 246-261.

1154 Jongmans, A.G., vanBreemen, N., Lundstrom, U., vanHees, P.A.W., Finlay, R.D.,
1155 Srinivasan, M., Unestam, T., Giesler, R., Melkerud, P.A., Olsson, M., 1997. Rock-eating fungi.
1156 *Nature* 389, 682-683.

1157 Kalinowski, B.E., Liermann, L.J., Brantley, S.L., Barnes, A., Pantano, C.G., 2000. X-
1158 ray photoelectron evidence for bacteria-enhanced dissolution of hornblende. *Geochim.*
1159 *Cosmochim. Acta* 64, 1331-1343.

1160 Kim, Y.H., Bae, B., Choung, Y.K., 2005. Optimization of biological phosphorus
1161 removal from contaminated sediments with phosphate-solubilizing microorganisms. *J. Biosci.*
1162 *Bioeng.* 99, 23-29.

1163 Klaminder, J., Lucas, R.W., Futter, M.N., Bishop, K.H., Kohler, S.J., Egnell, G.,
1164 Laudon, H., 2011. Silicate mineral weathering rate estimates: Are they precise enough to be
1165 useful when predicting the recovery of nutrient pools after harvesting? For. Ecol. Manage. 261,
1166 1-9.

1167 Knauss, K.G., Wolery, T.J., 1988. The dissolution kinetics of quartz as a function of pH
1168 and time at 70°C. Geochim. Cosmochim. Acta 52, 43-53.

1169 Lapanje, A., Wimmersberger, C., Furrer, G., Brunner, I., Frey, B., 2012. Pattern of
1170 elemental release during the granite dissolution can be changed by aerobic heterotrophic
1171 bacterial strains isolated from Damma glacier (central Alps) deglaciated granite sand. Microb.
1172 Ecol. 63, 865-882.

1173 Lasaga, A.C., 1998. Kinetic Theory in the Earth Sciences. Princeton University Press,
1174 New York.

1175 Lefèvre, Y., 1988. Les sols du bassin versant d'Aubure : caractérisation et facteurs de
1176 répartition. Ann. Sci. For. 45, 417-422.

1177 Lepleux, C., Turpault, M.P., Oger, P., Frey-Klett, P., Uroz, S., 2012. Correlation of the
1178 abundance of betaproteobacteria on mineral surfaces with mineral weathering in forest soils.
1179 Appl. Environ. Microbiol. 78, 7114-7119.

1180 Li, Z.B., Liu, L.W., Chen, J., Teng, H.H., 2016. Cellular dissolution at hypha- and spore-
1181 mineral interfaces revealing unrecognized mechanisms and scales of fungal weathering.
1182 Geology 44, 319-322.

1183 Lower, S.K., Hochella, M.F., Beveridge, T.J., 2001. Bacterial recognition of mineral
1184 surfaces: nanoscale interactions between *Shewanella* and α -FeOOH. Science 292, 1360-1363.

1185 Lucas, R.W., Klaminder, J., Futter, M.N., Bishop, K.H., Egnell, G., Laudon, H.,
1186 Hogberg, P., 2011. A meta-analysis of the effects of nitrogen additions on base cations:
1187 Implications for plants, soils, and streams. For. Ecol. Manage. 262, 95-104.

1188 Lüttge, A., Arvidson, R.S., Fischer, C., 2013. A Stochastic Treatment of Crystal
1189 Dissolution Kinetics. *Elements* 9, 183-188.

1190 Maher, K., DePaolo, D.J., Lin, J.C.-F., 2004. Rates of silicate dissolution in deep-sea
1191 sediment: In situ measurement using $^{234}\text{U}/^{238}\text{U}$ of pore fluids. *Geochim. Cosmochim. Acta*
1192 68, 4629-4648.

1193 Maher, K., Steefel, C.I., White, A.F., Stonestrom, D.A., 2009. The role of reaction
1194 affinity and secondary minerals in regulating chemical weathering rates at the Santa Cruz Soil
1195 Chronosequence, California. *Geochim. Cosmochim. Acta* 73, 2804-2831.

1196 Mailloux, B.J., Alexandrova, E., Keimowitz, A.R., Wovkulich, K., Freyer, G.A.,
1197 Herron, M., Stolz, J.F., Kenna, T.C., Pichler, T., Polizzotto, M.L., Dong, H., Bishop, M.,
1198 Knappett, P.S.K., 2009. Microbial mineral weathering for nutrient acquisition releases arsenic.
1199 *Appl. Environ. Microbiol.* 75, 2558-2565.

1200 Mitchell, A.C., Lafreniere, M.J., Skidmore, M.L., Boyd, E.S., 2013. Influence of
1201 bedrock mineral composition on microbial diversity in a subglacial environment. *Geology* 41,
1202 855-858.

1203 Negrel, P., Allegre, C.J., Dupre, B., Lewin, E., 1993. Erosion sources determined by
1204 inversion of major and trace element ratios and strontium isotopic ratios in river water - The
1205 congo basin case. *Earth Planet. Sci. Lett.* 120, 59-76.

1206 Newman, D.K., Kolter, R., 2000. A role for excreted quinones in extracellular electron
1207 transfer. *Nature* 405, 94-97.

1208 Nugent, M.A., Brantley, S.L., Pantano, C.G., Maurice, P.A., 1998. The influence of
1209 natural mineral coatings on feldspar weathering. *Nature* 395, 588-591.

1210 Odum, E.P., 1950. Bird populations of the Highlands (North Carolina) plateau in
1211 relation to plant succession and avian invasion. *Ecology* 31, 587-605.

1212 Oksanen J., F. Blanchet G., Kindt R., Legendre P., Minchin P. R., O'Hara R. B.,
1213 Simpson G. L., Solymos P., Stevens M. H. H. and Wagner H. (2013) Vegan: Community
1214 Ecology Package. R package version 2.0-8, <http://CRAN.R-project.org/package=vegan>.

1215 Or, D., Phutane, S., Dechesne, A., 2007. Extracellular polymeric substances affecting
1216 pore-scale hydrologic conditions for bacterial activity in unsaturated soils. *Vadose Zone J.* 6,
1217 298-305.

1218 Paces, T., 1983. Rate constants of dissolution derived from the measurements of mass
1219 balance in hydrological catchments. *Geochim. Cosmochim. Acta* 47, 1855-1863.

1220 Palandri, J.L., Kharaka, Y.K., 2004. A compilation of rate parameters of water-mineral
1221 interaction kinetics for application to geochemical modeling, in: Survey, U.S.G. (Ed.), U.S.
1222 Geological Survey, Open File Report. U.S. Geological Survey, Open File Report, p. 70.

1223 Pierret, M.C., Stille, P., Prunier, J., Viville, D., Chabaux, F., 2014. Chemical and U–Sr
1224 isotopic variations in stream and source waters of the Strengbach watershed (Vosges mountains,
1225 France). *Hydrol. Earth Syst. Sci.* 18, 3969-3985.

1226 Reguera, G., McCarthy, K.D., Mehta, T., Nicoll, J.S., Tuominen, M.T., Lovley, D.R.,
1227 2005. Extracellular electron transfer via microbial nanowires. *Nature* 435, 1098-1101.

1228 Rimstidt, J.D., Brantley, S.L., Olsen, A.A., 2012. Systematic review of forsterite
1229 dissolution rate data. *Geochim. Cosmochim. Acta* 99, 159-178.

1230 Roden, E.E., Kappler, A., Bauer, I., Jiang, J., Paul, A., Stoesser, R., Konishi, H., Xu,
1231 H.F., 2010. Extracellular electron transfer through microbial reduction of solid-phase humic
1232 substances. *Nat. Geosci.* 3, 417-421.

1233 Roelandt, C., Godderis, Y., Bonnet, M.P., Sondag, F., 2010. Coupled modeling of
1234 biospheric and chemical weathering processes at the continental scale. *Global Biogeochemical*
1235 *Cycles* 24.

1236 Saha, R., Saha, N., Donofrio, R.S., Bestervelt, L.L., 2013. Microbial siderophores: a
1237 mini review. *J. Basic Microbiol.* 53, 303-317.

1238 Singh, R., Beriault, R., Middaugh, J., Hamel, R., Chenier, D., Appanna, V.D., Kalyuzhnyi, S.,
1239 2005. Aluminum-tolerant *Pseudomonas fluorescens*: ROS toxicity and enhanced NADPH
1240 production. *Extremophiles* 9, 367-373.

1241 Sitch, S., Smith, B., Prentice, I.C., Arneth, A., Bondeau, A., Cramer, W., Kaplan, J.O.,
1242 Levis, S., Lucht, W., Sykes, M.T., Thonicke, K., Venevsky, S., 2003. Evaluation of ecosystem
1243 dynamics, plant geography and terrestrial carbon cycling in the LPJ dynamic global vegetation
1244 model. *Glob. Chang. Biol.* 9, 161-185.

1245 Solden, L., Lloyd, K., Wrighton, K., 2016. The bright side of microbial dark matter:
1246 lessons learned from the uncultivated majority. *Curr. Opin. Microbiol.* 31, 217-226.

1247 Steefel, C., Lasaga, A.C., 1994. A coupled model for transport of multiple chemical
1248 species and kinetic precipitation/dissolution reactions with application to reactive flow in single
1249 phase hydrothermal systems *Am. J. Sci.* 294, 529-592.

1250 Sverdrup, H., 1990. *The kinetics of Chemical Weathering*. Lund University Press, Lund,
1251 Sweden.

1252 Sverdrup, H., Warfvinge, P., 1993. Calculating field weathering rates using a
1253 mechanistic geochemical model PROFILE. *Appl. Geochem.* 8, 273-283.

1254 Sverdrup, H., Warfvinge, P., 1995. Estimating field weathering rates using laboratory
1255 kinetics, *Chemical Weathering Rates of Silicate Minerals*, pp. 485-541.

1256 Taylor, A.S., Blum, J.D., Lasaga, A.C., 2000. The dependence of labradorite dissolution
1257 and Sr isotope release rates on solution saturation state. *Geochim. Cosmochim. Acta* 64, 2389-
1258 2400.

1259 Tester, J.W., Worley, W.G., Robinson, B.A., Grigsby, C.O., Feerer, J.L., 1994.
1260 Correlating quartz dissolution kinetics in pure water from 25 to 625°C. *Geochim. Cosmochim.*
1261 Acta 58, 2407-2420.

1262 Ullman, W.J., Kirchman, D.L., Welch, S.A., Vandevivere, P., 1996. Laboratory
1263 evidence for microbially mediated silicate mineral dissolution in nature. *Chem. Geol.* 132, 11-
1264 17.

1265 Uroz, S., Calvaruso, C., Turpault, M.-P., Frey-Klett, P., 2009. Mineral weathering by
1266 bacteria: ecology, actors and mechanisms. *Trends Microbiol.* 17, 378-387.

1267 Uroz, S., Calvaruso, C., Turpault, M.P., Pierrat, J.C., Mustin, C., Frey-Klett, P., 2007.
1268 Effect of the mycorrhizosphere on the genotypic and metabolic diversity of the bacterial
1269 communities involved in mineral weathering in a forest soil. *Appl. Environ. Microbiol.* 73,
1270 3019-3027.

1271 Uroz, S., Kelly, L.C., Turpault, M.P., Lepleux, C., Frey-Klett, P., 2015. The
1272 Mineralosphere concept: mineralogical control of the distribution and function of mineral-
1273 associated bacterial communities. *Trends Microbiol.* 23, 751-762.

1274 Uroz, S., Turpault, M.P., Delaruelle, C., Mareschal, L., Pierrat, J.C., Frey-Klett, P.,
1275 2012. Minerals affect the specific diversity of forest soil bacterial communities. *Geomicrobiol.*
1276 J.29, 88-98.

1277 van der Heijden, G., Legout, A., Pollier, B., Mareschal, L., Turpault, M.P., Ranger, J.,
1278 Dambrine, E., 2013. Assessing Mg and Ca depletion from broadleaf forest soils and potential
1279 causes - A case study in the Morvan Mountains. *For. Ecol. Manage.* 293, 65-78.

1280 van Scholl, L., Kuyper, T.W., Smits, M.M., Landeweert, R., Hoffland, E., van Breemen,
1281 N., 2008. Rock-eating mycorrhizas: their role in plant nutrition and biogeochemical cycles.
1282 *Plant Soil* 303, 35-47.

1283 Vassilev, N., Vassileva, M., Nikolaeva, I., 2006. Simultaneous P-solubilizing and
1284 biocontrol activity of microorganisms: potentials and future trends. *Appl. Microbiol.*
1285 *Biotechnol.* 71, 137-144.

1286 Violette, A., Godd ris, Y., Mar chal, J.-C., Riotte, J., Oliva, P., Kumar, M.S.M., Sekhar,
1287 M., Braun, J.-J., 2010. Modelling the chemical weathering fluxes at the watershed scale in the
1288 Tropics (Mule Hole, South India): Relative contribution of the smectite/kaolinite assemblage
1289 versus primary minerals. *Chem. Geol.* 277, 42-60.

1290 Viville, D., Chabaux, F., Stille, P., Pierret, M.C., Gangloff, S., 2012. Erosion and
1291 weathering fluxes in granitic basins: The example of the Strengbach catchment (Vosges massif,
1292 eastern France). *Catena* 92, 122-129.

1293 Walters, W.A., Caporaso, J.G., Lauber, C.L., Berg-Lyons, D., Fierer, N., Knight, R.,
1294 2011. PrimerProspector: de novo design and taxonomic analysis of barcoded polymerase chain
1295 reaction primers. *Bioinformatics* 27, 1159-1161.

1296 Ward, J.H., 1963. Hierarchical Grouping to Optimize an Objective Function. *J. Am.*
1297 *Stat. Assoc.* 58, 236-244.

1298 Warfvinge, P., Sverdrup, H., 1988. Soil liming as a measure to mitigate acid
1299 runoff. *Water Resour. Res.* 24, 701-712.

1300 Warfvinge, P., Sverdrup, H., 1992. Calculating critical loads of acid deposition with
1301 PROFILE - a steady-state soil chemistry model. *Water, Air, Soil Pollut.* 63, 119-143.

1302 Weber, K.A., Achenbach, L.A., Coates, J.D., 2006. Microorganisms pumping iron:
1303 anaerobic microbial iron oxidation and reduction. *Nat. Rev. Microbiol.* 4, 752-764.

1304 Welch, S.A., Barker, W.W., Banfield, J.F., 1999. Microbial extracellular
1305 polysaccharides and plagioclase dissolution. *Geochim. Cosmochim. Acta* 63, 1405-1419.

1306 Welch, S.A., Ullman, W.J., 1993. The effect of organic acids on plagioclase dissolution
1307 rates and stoichiometry. *Geochim. Cosmochim. Acta* 57, 2725-2736.

1308 White, A.F., Brantley, S.L., 2003. The effect of time on the weathering of silicate
1309 minerals: why do weathering rates differ in the laboratory and field? *Chem. Geol.* 202, 479-
1310 506.

1311 Wild, B., Daval, D., Guyot, F., Knauss, K.G., Pollet-Villard, M., Imfeld, G., 2016. pH-
1312 dependent control of feldspar dissolution rate by altered surface layers. *Chem. Geol.* 442, 148-
1313 159.

1314 Wild, B., Imfeld, G., Guyot, F., Daval, D., 2018. Early stages of bacterial community
1315 adaptation to silicate aging. *Geology* 46, 555-558.

1316 Wu, L., Jacobson, A.D., Chen, H.-C., Hausner, M., 2007. Characterization of elemental
1317 release during microbe-basalt interactions at T=28 degrees C. *Geochim. Cosmochim. Acta* 71,
1318 2224-2239.

1319 Wu, L., Jacobson, A.D., Hausner, M., 2008. Characterization of elemental release
1320 during microbe-granite interactions at T=28 °C. *Geochim. Cosmochim. Acta* 72, 1076-1095.

1321 Yarza, P., Yilmaz, P., Pruesse, E., Glockner, F.O., Ludwig, W., Schleifer, K.-H.,
1322 Whitman, W.B., Euzéby, J., Amann, R., Rossello-Mora, R., 2014. Uniting the classification of
1323 cultured and uncultured bacteria and archaea using 16S rRNA gene sequences. *Nat. Rev.*
1324 *Microbiol.* 12, 635-645.

1325 Yeh, G.T., Tripathi, V.S., 1991. A Model for Simulating Transport of Reactive
1326 Multispecies Components: Model Development and Demonstration. *Water Resour. Res.* 27,
1327 3075-3094.

1328 Yu, C., Lavergren, U., Peltola, P., Drake, H., Bergbäck, B., Åström, M.E., 2014.
1329 Retention and transport of arsenic, uranium and nickel in a black shale setting revealed by a
1330 long-term humidity cell test and sequential chemical extractions. *Chem. Geol.* 363, 134-144.

1331 Zhu, C., Liu, Z., Schaefer, A., Wang, C., Zhang, G., Gruber, C., Ganor, J., Georg, R.B.,
1332 2014. Silicon Isotopes as a New Method of Measuring Silicate Mineral Reaction Rates at
1333 Ambient Temperature. *Procedia Earth and Planet. Sci.* 10, 189-193.

1334

1335

1336 **8. FIGURE CAPTIONS**

1337

1338 Fig. 1: Compartments of the critical zone probed at the Strengbach catchment (A). Soil profile
1339 of the beech plot (B) and corresponding reactivity probes after 20 months of incubation into the
1340 A horizon (C) and the C horizon (D). Overview of the setup used to expose samples to
1341 atmospheric weathering (E) onto a Polytetrafluoroethylene (PTFE) plate (F). Reactivity probe
1342 after 20 months of incubation at the weather station (G). Experimental setup used to immerse
1343 samples into the Strengbach stream at the outlet (H) with flow-through PTFE holders (I).
1344 Reactivity probe after 20 months of incubation into the Strengbach stream (J). White and black
1345 crosses indicate the locations of the samples.

1346

1347 Fig. 2: Exchangeable Mg (A) and Ca (B) as determined by ammonium acetate extractions on
1348 samples of the soil profile of the beech plot collected on 11/18/2013 and 12/02/2014 (see Table
1349 A.3). For comparison, green and orange plots represent corresponding concentrations measured
1350 at the experimental plot of Breuil-Chenue (Morvan, France) before and 30 years after
1351 deforestation respectively (van der Heijden *et al.*, 2013).

1352

1353 Fig. 3: Labradorite sample collected after 9 months of incubation in the C horizon of the soil
1354 profile of the beech plot at the Strengbach catchment. Stereo microscope image acquired before
1355 removal of the Room Temperature Vulcanizing (RTV) glue mask (A), vertical scanning

1356 interferometry (VSI) surface topography after cleaning (B) and interpretation in terms of
1357 surface retreat overlaid on stitched VSI images before removal of the RTV glue mask
1358 (visible inside the circled area) of the same portion of the sample (C). Black arrowheads in (B)
1359 indicate zones where the global retreat of the surface at the previous location of the mask is
1360 visible. White arrows indicate another boundary of the mask indicated by a residue of RTV
1361 glue. Striped zone in (C) correspond to a location where natural fluid circulation likely occurred
1362 (see text).

1363

1364 Fig. 4: Olivine samples after 9 months of incubation in the A horizon of the soil profile of the
1365 beech plot at the Strengbach catchment. Stereo microscope image acquired before removal of
1366 the RTV glue mask (A) and stitched VSI images of the surface after cleaning (B). Dashed lines
1367 indicate the boundary of zones interpreted in (C) as portions of the olivine surface that were
1368 either masked (1), including traces of possible fluid circulation (2), or the rest of the mineral
1369 surface exposed to the soil environment (3). Red box in C indicates the portion of the surface
1370 imaged by stereo microscope right after incubation (D) or by VSI before (E) and after (F) 9
1371 months of incubation. Striped zone in (D), (E) and (F) correspond to the masked area. Profiles
1372 at the boundary between zones 2 and 3 and zones 1 and 2 (indicated by a red arrowhead) before
1373 (in blue) and after (in red) 9 months of incubation are reported in (G) and (H) respectively..

1374

1375 Fig. 5: Detail of the surface topography of an olivine reactivity probe before (A) and after (B)
1376 9 months of incubation in the A horizon of the soil profile at the beech plot. Superposition of
1377 profiles before (black) and after (red) incubation (C) and corresponding surface retreat (D). This
1378 analysis reveals a global retreat of the surface (red arrow, C; dashed area, D) and local alteration
1379 features (green arrow, C; dotted area, D).

1380

1381 Fig. 6: Detail of the surface topography of an olivine reactivity probe after 9 months of
1382 incubation in the A horizon of the soil profile of the
1383 plot (A, C). Its interpretation in terms of weathering fluxes, as estimated from topography and
1384 rate spectra (D, E) following the approach developed in (Fischer et al., 2012), is displayed (B).
1385 It reveals zones impacted by the global retreat of the surface (green) with respect to the initial
1386 masked surface area (black, M) and local alteration features (red). The contribution of zones
1387 related to the initial topography is highlighted in grey.

1388

1389 Fig. 7: Temporal variations of pH (A), temperature (B), and dissolution rates (C) of olivine and
1390 labradorite modeled by WITCH for two soil horizons at the beech plot of the Strengbach
1391 catchment. The greyed areas correspond to the incubation period of the probes.

1392

1393 Fig. 8: Relative proportions of bacterial phyla analyzed in the environmental probes incubated
1394 in several compartments of the critical zone at the Strengbach catchment. Mean values over all
1395 samples incubated at a given location. “Others” category gathers the 20 less represented phyla
1396 together with sequences which could not be classified with a sufficient degree of confidence.

1397

1398 Fig. 9: Statistical analyses of the composition of microbial communities of the environmental
1399 probes incubated at the weather station (A,B), in the A horizon (C,D), in the C horizon (E,F),
1400 and in the stream (G,H). Analyzed samples include the mineralosphere of labradorite (L),
1401 olivine (O) and quartz (Q), as well as microbial communities from environmental matrices (E,
1402 either soil or stream sediments) and empty test bags (B). Trees correspond to the aggregation
1403 of OTUs at the species level with the Ward method on the basis of Bray-Curtis distances (A, C,
1404 E, G). Principal coordinate analyses (PCoA) of the relative abundance of the 16S rRNA genes
1405 with colors corresponding to the clusters determined with the Ward method. Crosses match to

1406 *a posteriori* projection of OTUs corresponding to *Collimonas* sp. (1), *Burkholderia* sp. (2),
1407 *Pseudomonas* sp. (3), *Janthinobacterium* sp. (4), *Leifsonia* sp. (5), *Polaromonas* sp. (6),
1408 *Sphingomonas* sp. (7), *Arthrobacter* sp. (8).

1409

1410 Fig. 10: Detail of the surface topography of an olivine reactivity probe before (A) and after (B)
1411 20 months of incubation at the weather station. Superposition of profiles before (black) and
1412 after (red) incubation (C) and corresponding surface retreat (D). 3D plot of the surface after
1413 incubation (B) with masked (M) zones (E).

1414

1415 Fig. 11: Evolutions of the $f(\Delta G_r)$ term, which describes the effect of the distance from
1416 equilibrium of the solution on mineral dissolution rate, and of the surface retreats for olivine
1417 and labradorite predicted by the WITCH model for the A and C horizons of the soil profile (A).
1418 The period highlighted in grey corresponds to the incubation of the samples. The $f(\Delta G_r)$
1419 function is equal to ~ 1 for all conditions except for labradorite in the C horizon when the *rate* –
1420 ΔG_r relation is described by the model of Taylor *et al.* (2000). Squares and diamonds in panels
1421 (B)-(D) represent *measured* surface retreats for samples incubated in the A and C horizons,
1422 respectively. Continuous curves represent *predicted* surface retreats based on outputs from the
1423 WITCH model. Corrected curves take into account fluid-mineral contact time and are based on
1424 ($f_2(\Delta G_r)$) function (see text). This figure stresses the amplitude of the field-laboratory
1425 discrepancy. The error bars are smaller than the size of symbols.

1426

1427 Fig. 12: Relative proportions of *Pseudomonas* sp., *Burkholderia* sp., *Collimonas* sp. (A), and
1428 *Arthrobacter* sp., *Leifsonia* sp., *Janthinobacterium* sp., et *Polaromonas* sp. (B), in the
1429 mineralospheres of quartz (Q), labradorite (L) and olivine (O), as well as in environmental
1430 samples (E) or empty bags (B). This figure illustrates that the proportion of genera known for

1431 their mineral weathering ability in pedological context is increased in the microbial
1432 communities of the environmental probes compared to those recovered from their respective
1433 surrounding environmental matrix.

1434

1435 **9. TABLE CAPTIONS**

1436

1437 Table 1: Global retreat of the surface of labradorite Δ_z and associated dissolution rate r
1438 measured *in-situ* in the field (F) or issued from WITCH simulations from kinetic rate laws
1439 determined in the laboratory (L), based on the transition state theory. Values between
1440 parentheses are based on a rate - ΔG_r relationship by Taylor *et al.* (2000). Predicted extent of
1441 reaction ξ and associated field-laboratory discrepancies $\Delta_{L/F}$. n.d. could not be estimated based
1442 on the methodology proposed here, since expected retreats were lower than measurable retreats
1443 due to the quality of the polishing of the corresponding samples.

1444

1445 Table 2: Global retreat of the surface of olivine Δ_z and associated dissolution rate r measured
1446 *in-situ* in the field (F) or issued from WITCH simulations from kinetic rate laws determined in
1447 the laboratory (L), based on the transition state theory. Predicted extent of reaction ξ and
1448 associated field-laboratory discrepancies $\Delta_{L/F}$. * retreat determined on a zone with no specific
1449 feature proving fluid circulation. ** possibly of biotic origin (see text).

Table 1

Sample	Context	incubation duration [months]	Labradorite							
			Δ_Z^F [nm]	r_F [mol.m ⁻² .s ⁻¹]	T [°C]	pH	Δ_Z^L [nm]	r_L [mol.m ⁻² .s ⁻¹]	ξ [mol.m ⁻²]	$\Delta_{L/F}$
ML9	Weather Station	9	2*	8.59E-13	7.1	5.4	4.4	1.88E-12	4.49E-05	2.2
ML20	Weather Station	20	2*	3.84E-13	7.1	5.4	9.8	1.88E-12	1.01E-04	4.9
AL9a	A horizon	9	2*	8.59E-13	6.1	4.2	30.6	1.31E-11	2.93E-04	15.3
AL9b	A horizon	9	4.5	1.99E-12	6.1	4.2	30.3	1.34E-11	2.87E-04	6.7
AL20	A horizon	20	1.1*	2.11E-13	6.1	4.2	59.4	1.14E-11	5.68E-04	54.0
CL9a	C horizon	9	1.5*	6.44E-13	6.1	5.2	6.2 (1.7)	2.68E-12 (7.24E-13)	3.26E-05	4.1 (1.1)
CL9b	C horizon	9	1*	4.42E-13	6.1	5.2	6.1 (1.6)	2.72E-12 (7.24E-13)	3.16E-05	6.1 (1.6)
CL9c	C horizon	9	2.5*	1.11E-12	6.1	5.2	6.1 (1.6)	2.72E-12 (7.24E-13)	3.16E-05	2.4 (0.7)
CL20	C horizon	20	1.5*	2.88E-13	6.1	5.2	11.2 (3.1)	2.17E-12 (5.85E-13)	5.95E-05	7.5 (2.0)
EL9a	Stream	9	5*	2.15E-12	5.8	6.5	0.8	3.55E-13	8.45E-06	n.d.
EL9b	Stream	9	4*	1.77E-12	5.8	6.5	0.8	3.55E-13	8.21E-06	n.d.
EL20	Stream	20	1*	1.92E-13	5.8	6.5	1.8	3.55E-13	1.89E-05	1.8

Table 2

Sample	Context	incubation duration [months]	Olivine							
			Δ_Z^F [nm]	r_F [mol.m ⁻² .s ⁻¹]	T [°C]	pH	Δ_Z^L [nm]	r_L [mol.m ⁻² .s ⁻¹]	ξ [mol.m ⁻²]	$\Delta_{L/F}$
MO9	Weather Station	9	1*	9.38E-13	7.1	5.4	83.8	7.87E-11	1.70E-03	84
MO20	Weather Station	20	171	7.17E-11	7.1	5.4	187.7	7.87E-11	3.82E-03	1
AO9	A horizon	9	24.19	2.27E-11	6.1	4.2	407.2	3.82E-10	8.53E-03	17
AO20	A horizon	20	3**	1.26E-12	6.1	4.2	809.6	3.39E-10	1.71E-02	270
CO9	C horizon	9	1.5	1.41E-12	6.1	5.2	112.1	1.05E-10	1.48E-03	75
CO20	C horizon	20	2*	8.38E-13	6.1	5.2	211.1	8.85E-11	2.75E-03	106
EO9	Stream	9	2.5	2.35E-12	5.8	6.5	21.7	2.04E-11	4.53E-04	9
EO20	Stream	20	2.5*	1.05E-12	5.8	6.5	48.6	2.04E-11	1.01E-03	19

Figure 1

[Click here to download high resolution image](#)

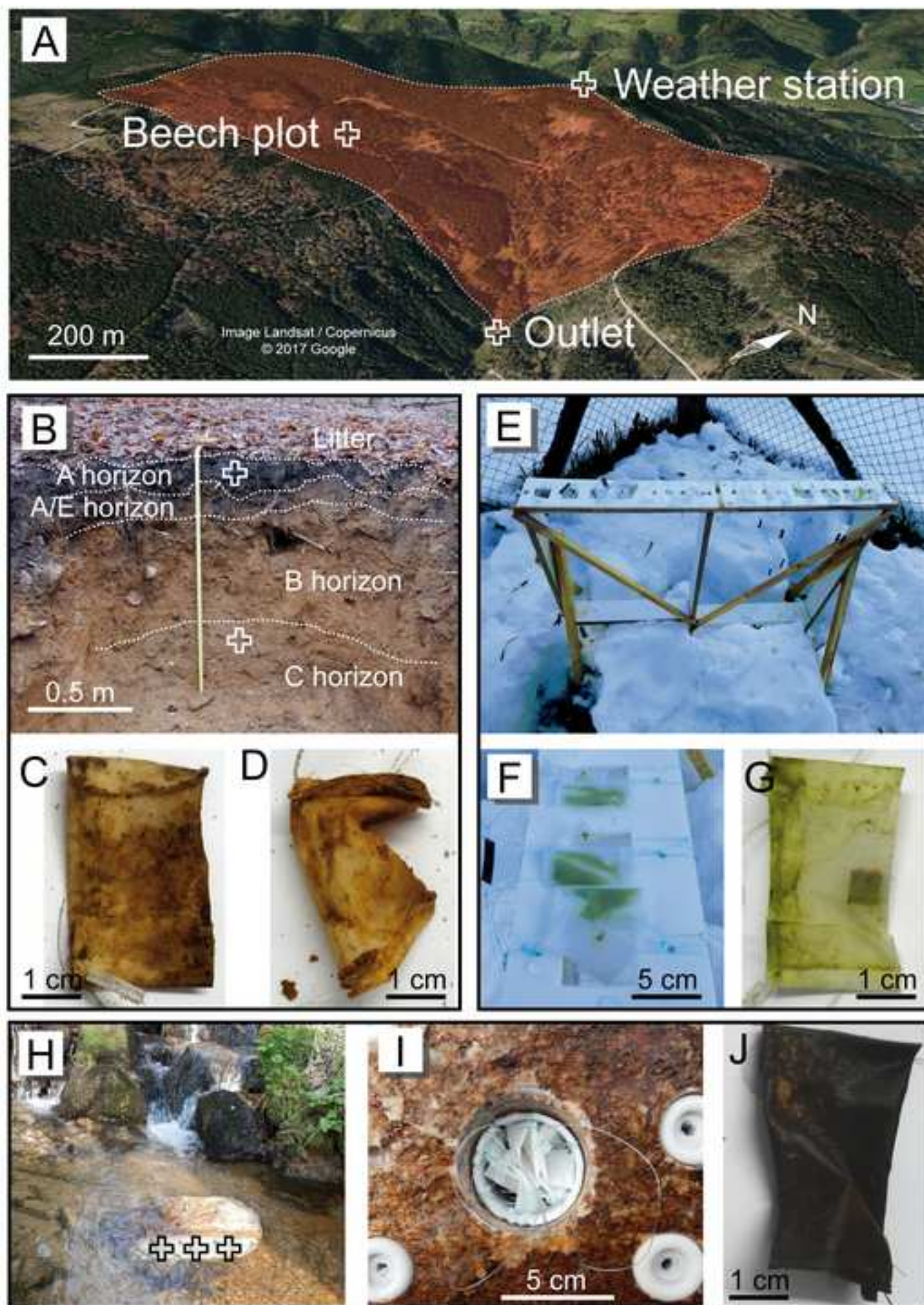


Figure 2
[Click here to download high resolution image](#)

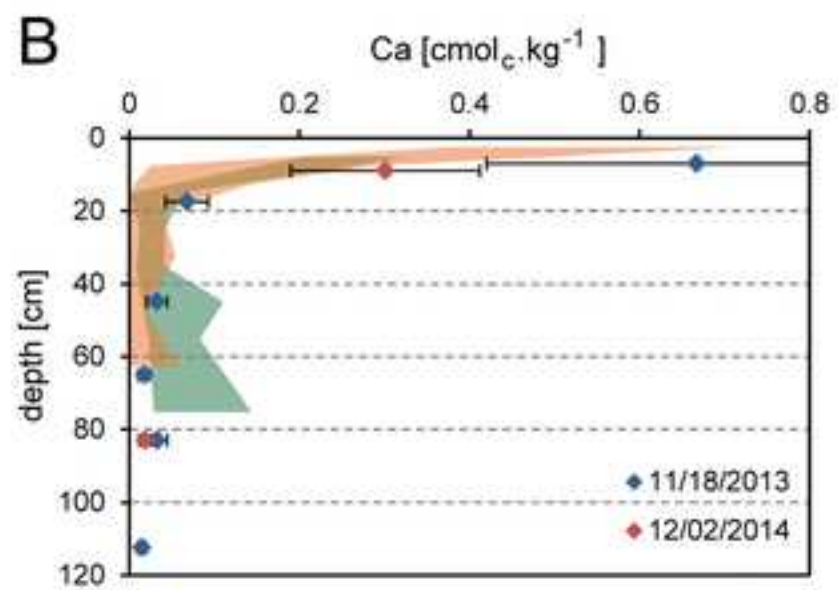
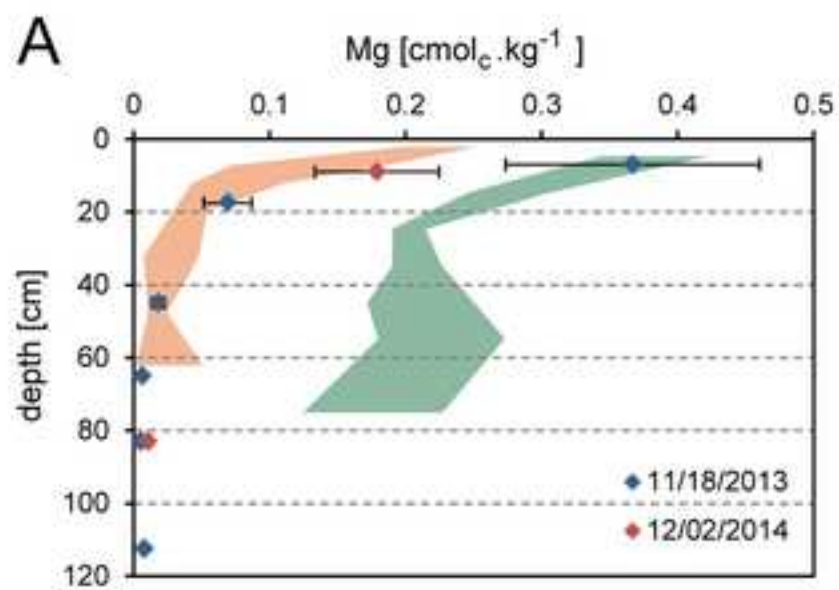


Figure 3
[Click here to download high resolution image](#)

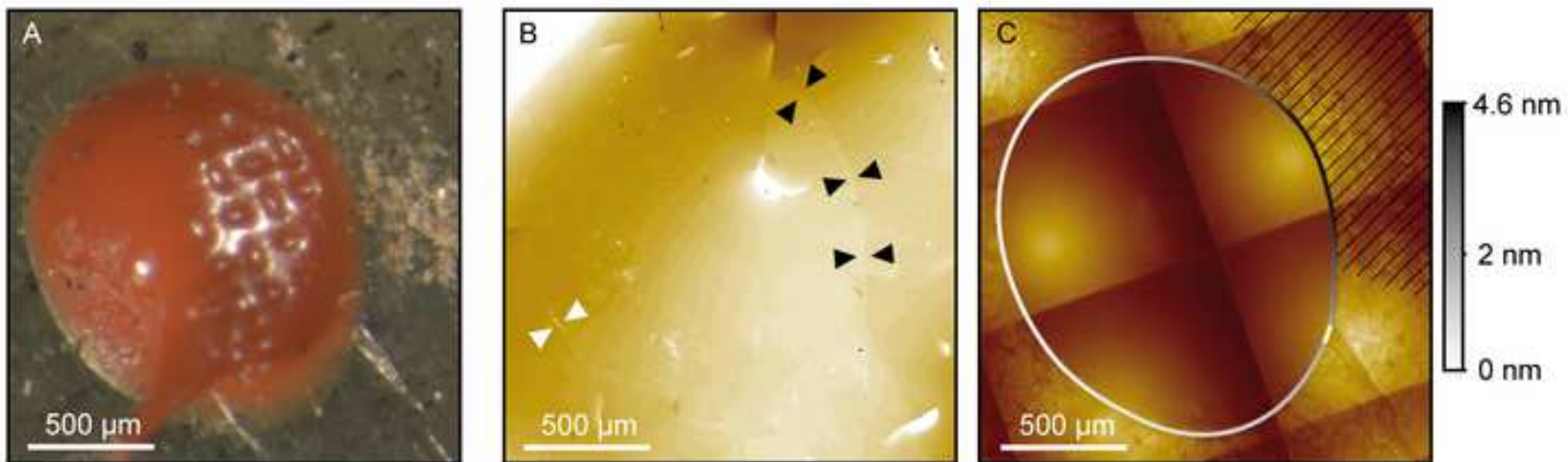


Figure 4
[Click here to download high resolution image](#)

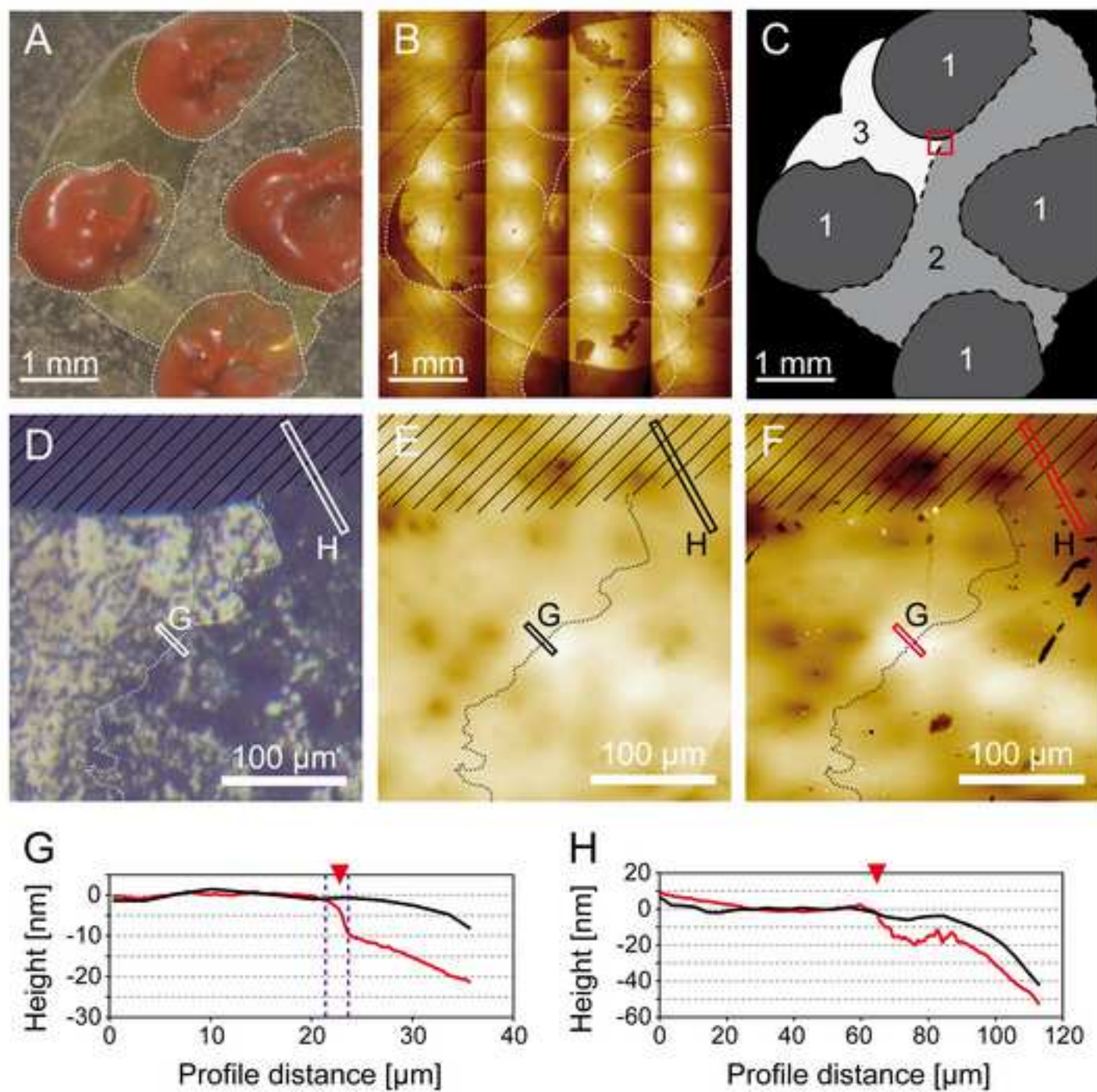


Figure 5
[Click here to download high resolution image](#)

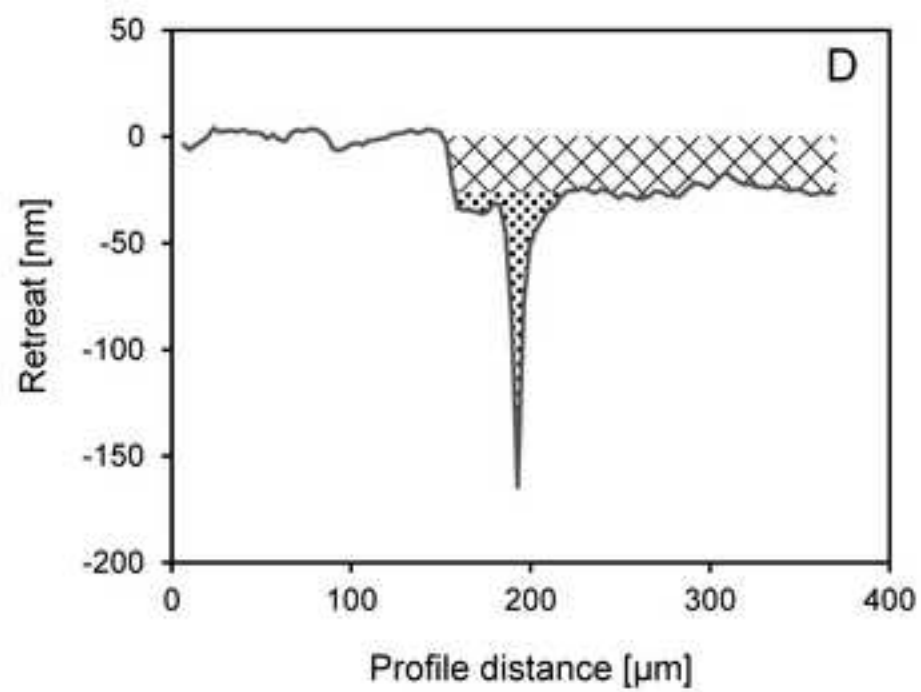
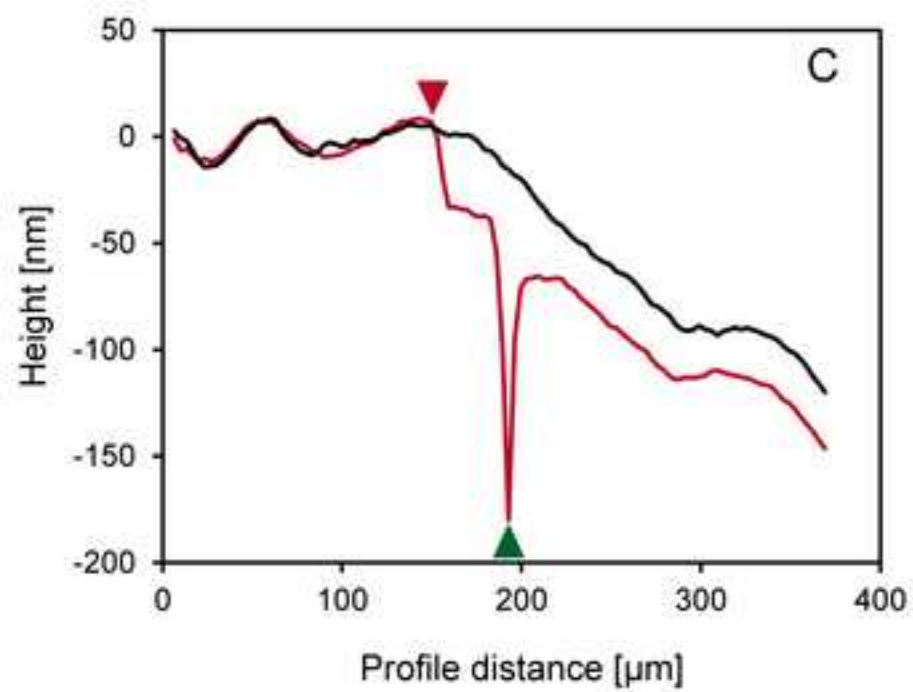
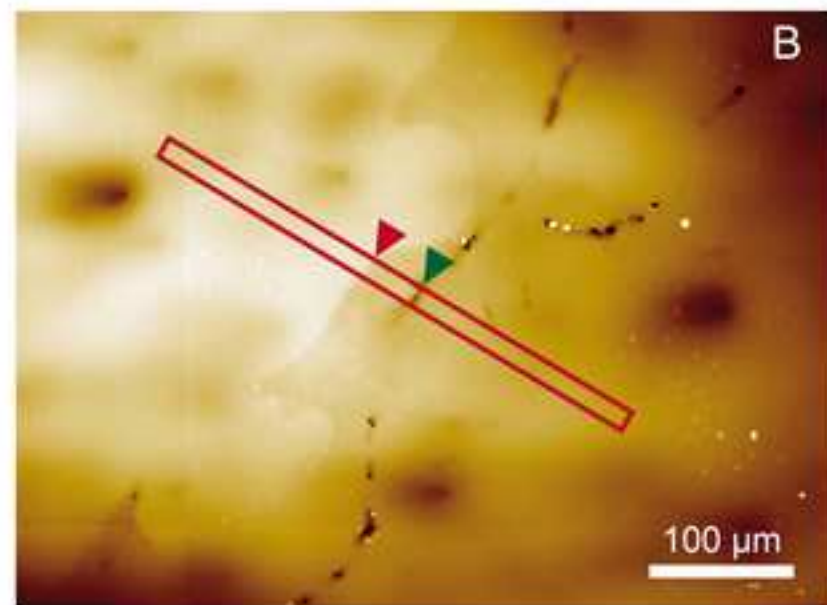
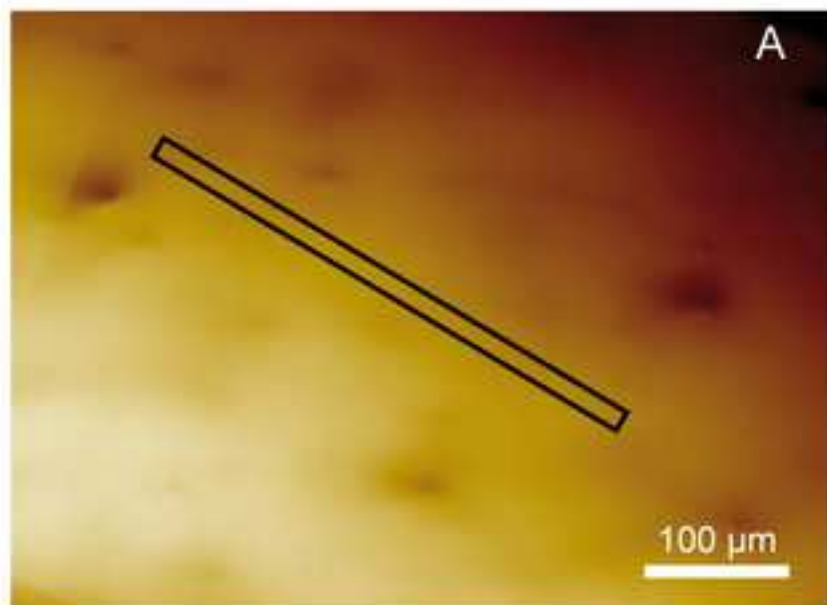


Figure 6
[Click here to download high resolution image](#)

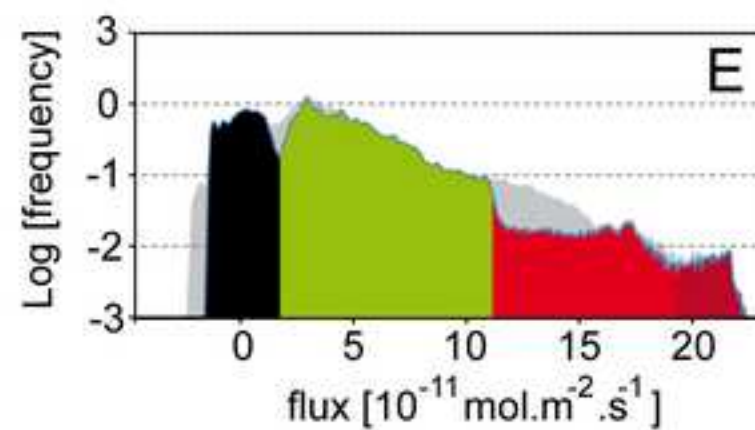
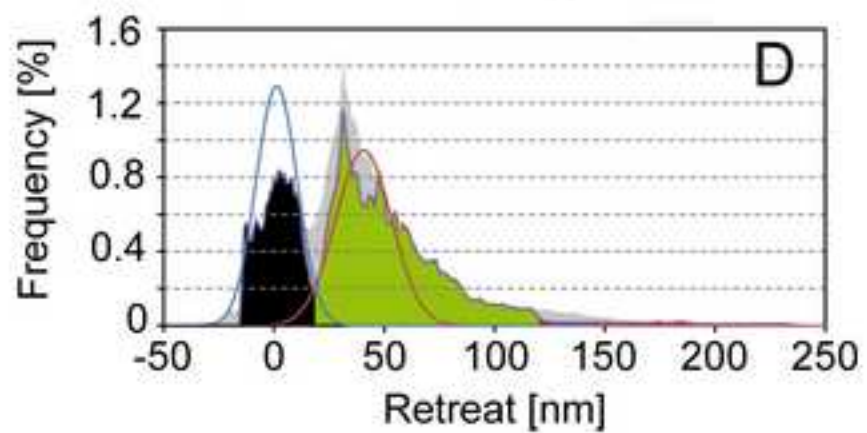
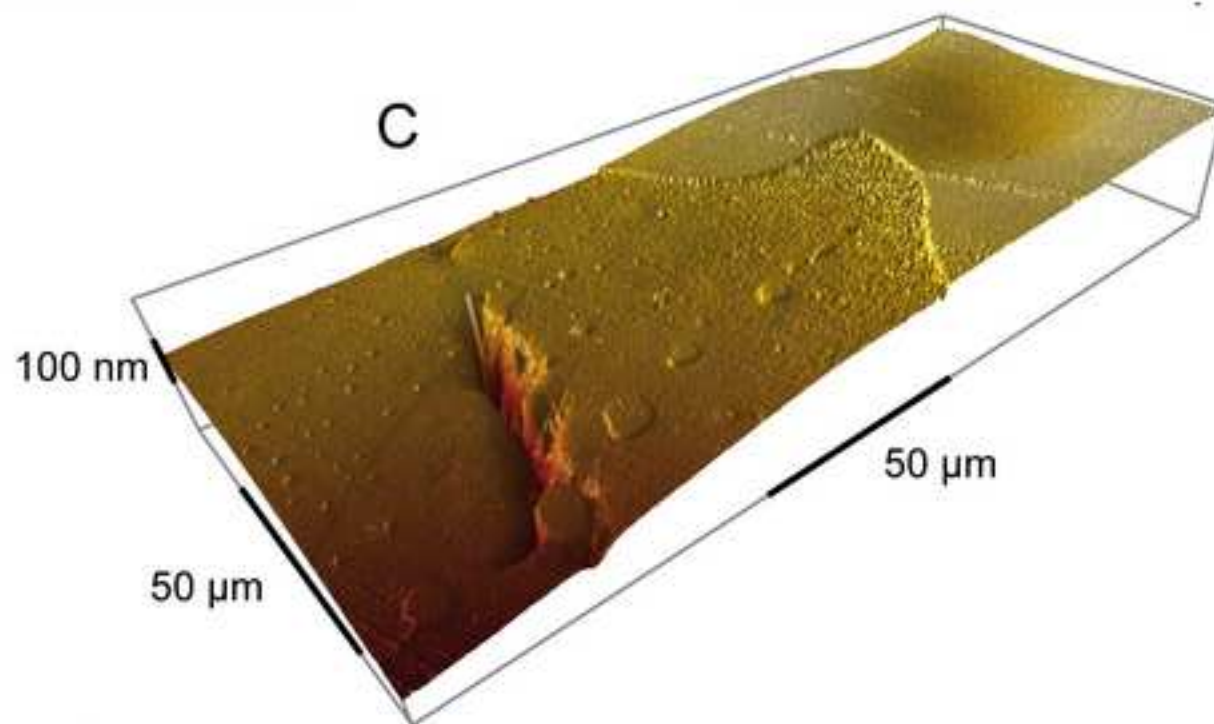


Figure 7
[Click here to download high resolution image](#)

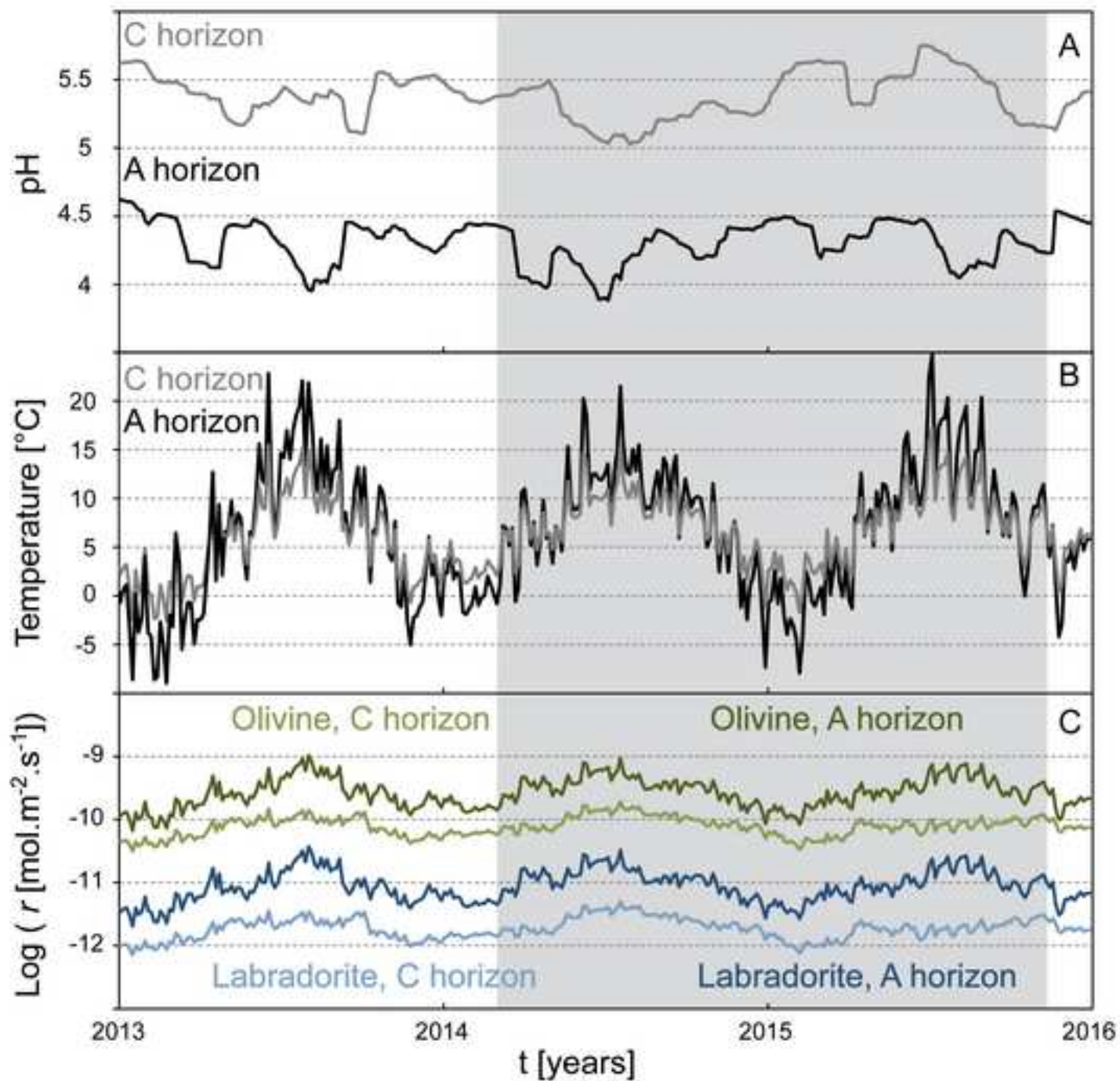


Figure 8
[Click here to download high resolution image](#)

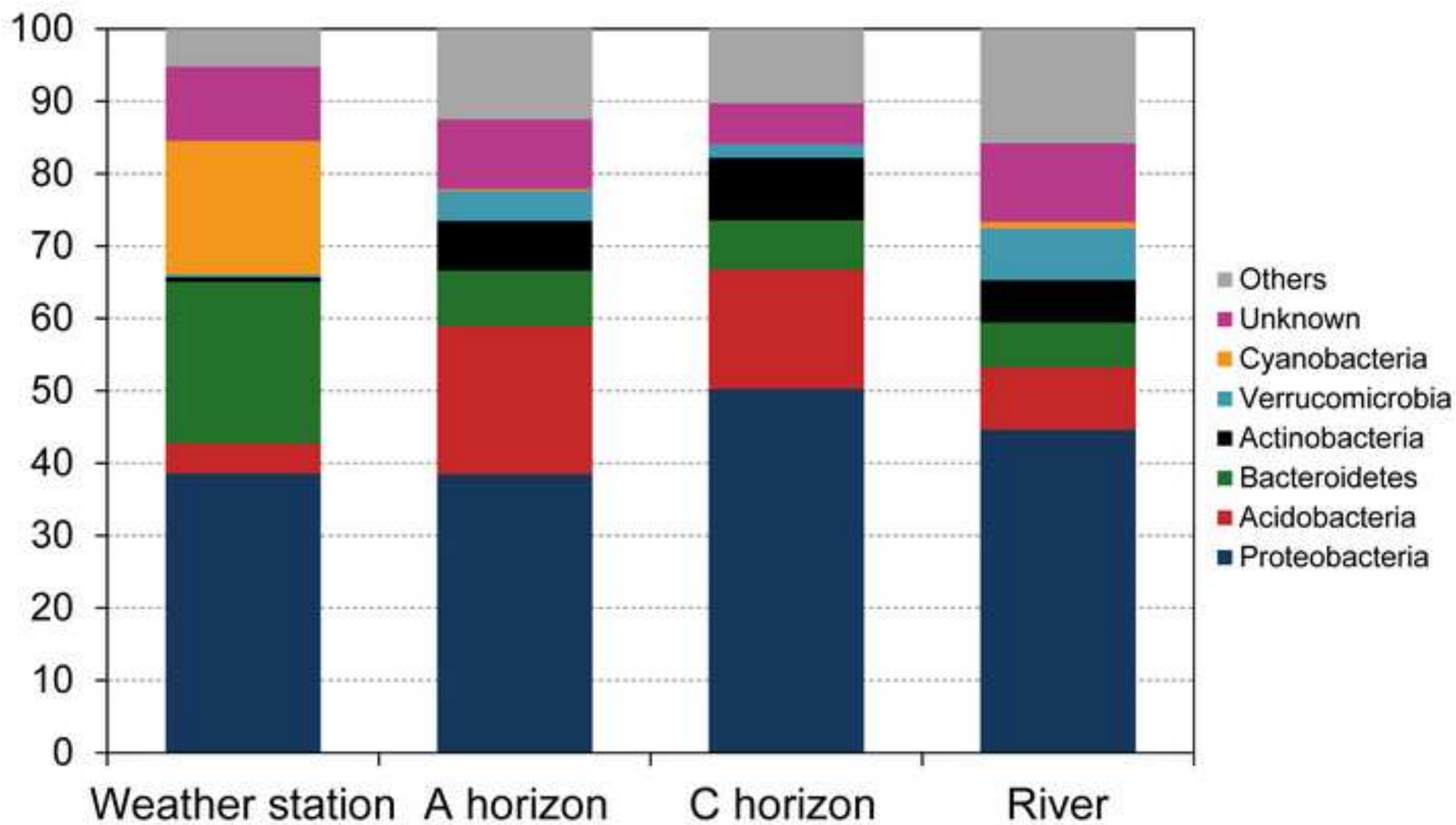


Figure 9

[Click here to download high resolution image](#)

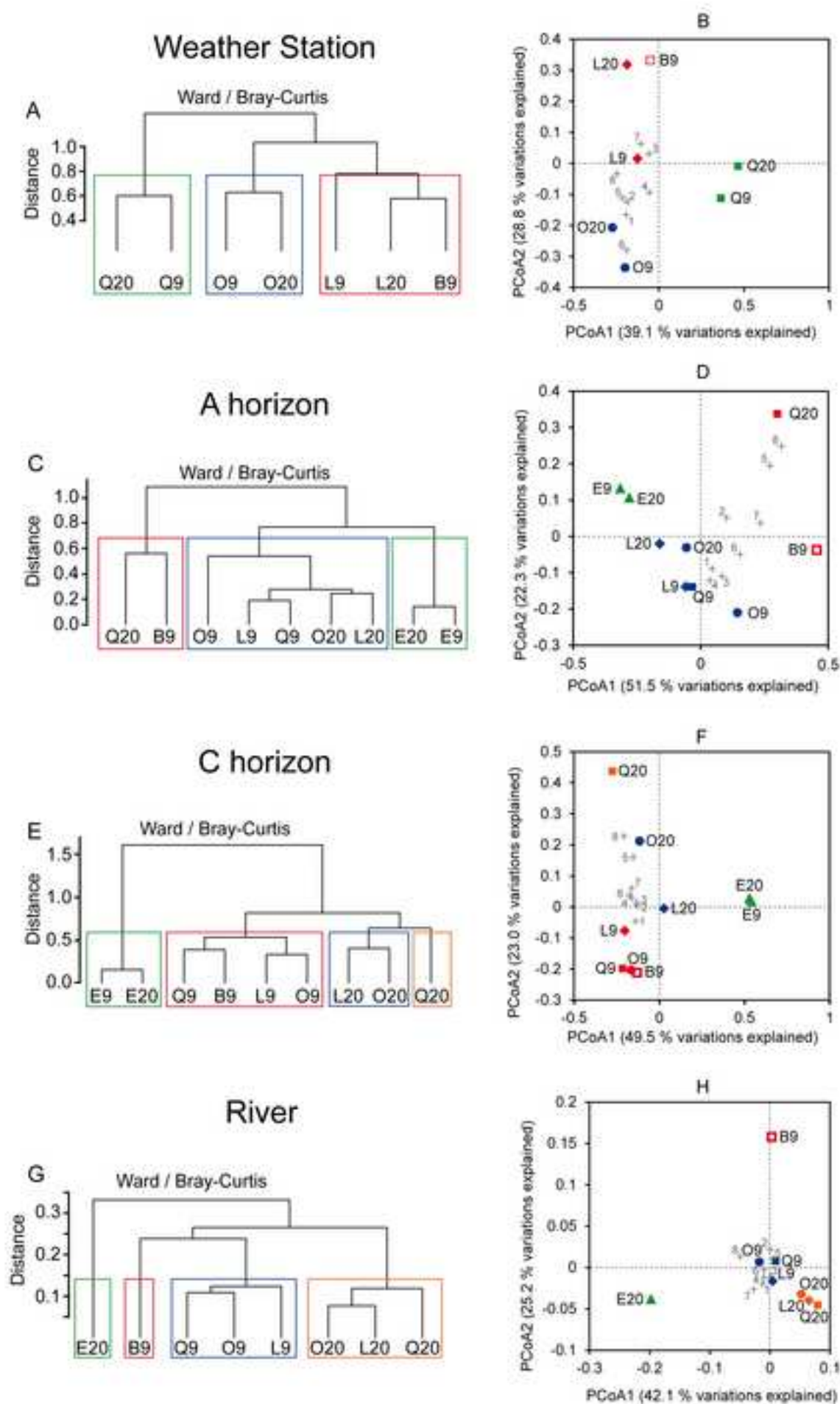


Figure 10
[Click here to download high resolution image](#)

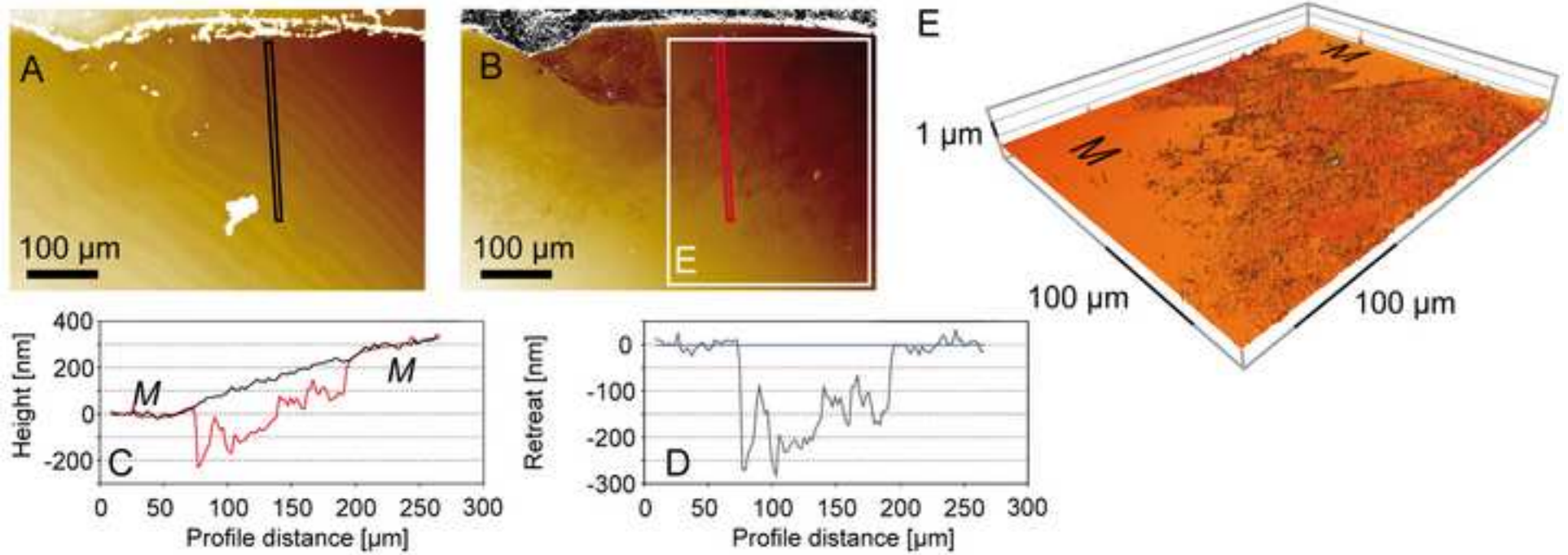


Figure 11

[Click here to download high resolution image](#)

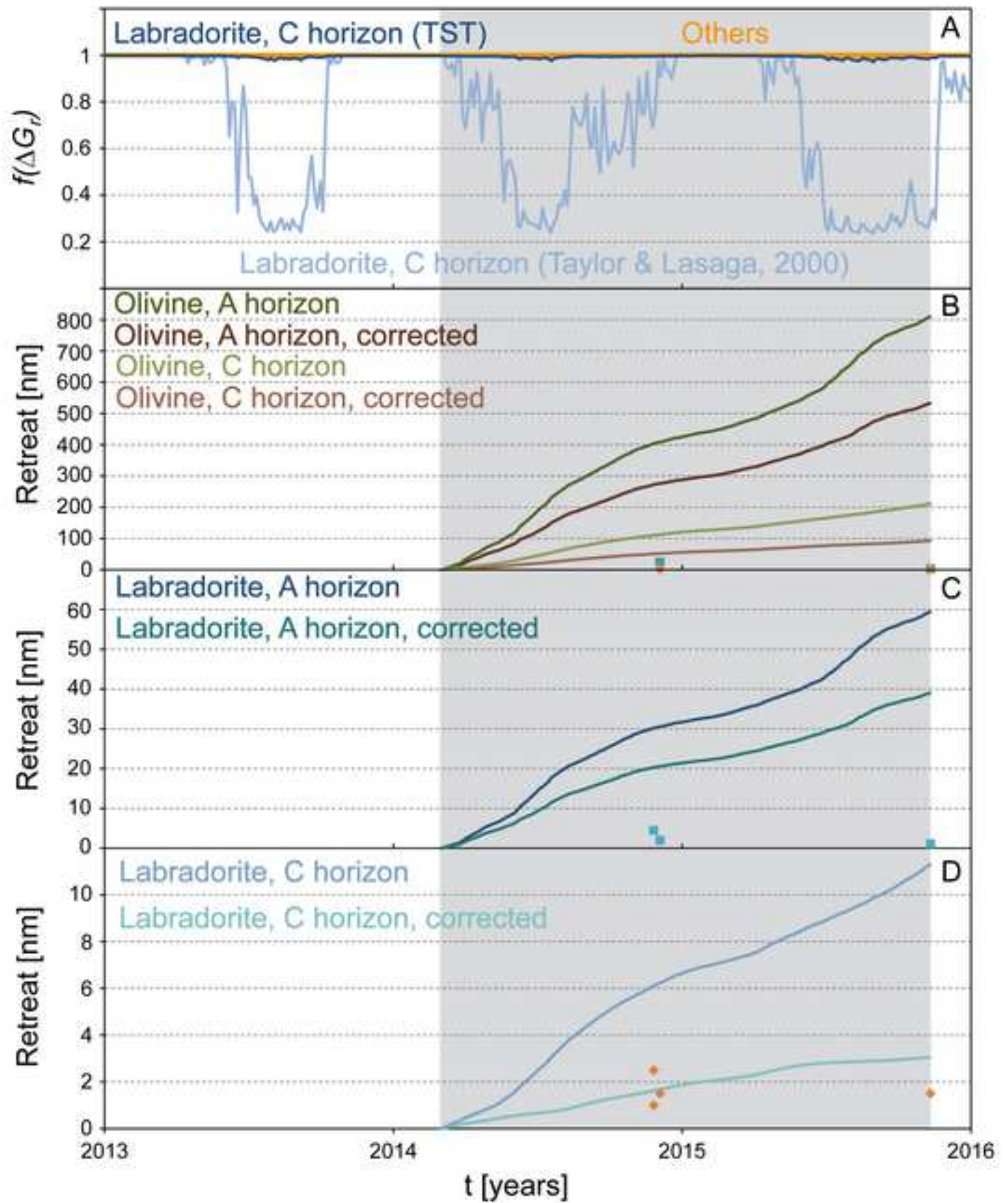


Figure 12

[Click here to download high resolution image](#)

